Madden-Julian Oscillations Seen in the Upper-Troposphere Vorticity Field: Interactions with Rossby Wave Trains

Jun-Ichi Yano, Danyang Wang, Yanluan Lin

Madden–Julian Oscillations Seen in the Upper-Troposphere Vorticity Field: Interactions with Rossby Wave Trains

DANYANG WANG

Key Laboratory for Earth System Modeling, Ministry of Education, Department of Earth System Science, Tsinghua University, and Joint Center for Global Change Studies, Beijing, China

JUN-ICHI YANO

CNRM, Météo-France, and CNRS, UMR 3589, Toulouse, France

YANLUAN LIN

Key Laboratory for Earth System Modeling, Ministry of Education, Department of Earth System Science, Tsinghua University, and Joint Center for Global Change Studies, Beijing, China

(Manuscript received 20 June 2018, in final form 27 February 2019)

ABSTRACT

The vorticity variability associated with the Madden–Julian oscillation (MJO) is examined. The analysis is focused on the 150-hPa pressure level, because a clear dipolar-vortex signal, reminiscent of the theoretically proposed strongly nonlinear solitary Rossby wave solution (albeit with the opposite sign), is seen in raw data at that level. A local empirical orthogonal function (EOF) analysis over the equatorial region of the Eastern Hemisphere (0°–180°E) identifies the two principal components representing an eastward propagation of a dipolar vortex trapped to the equator. Association of this propagation structure with the moist convective variability of the MJO is demonstrated by regressing the outgoing longwave radiation (OLR) against this EOF pair. The obtained evolution of the OLR field is similar to the one obtained by a direct application of the EOF to the OLR. A link of the local vorticity variability associated with the MJO to the global dynamics is further investigated by regressing the global vorticity field against the time series of the identified local EOF pair. The Rossby wave trains tend to propagate toward the Indian Ocean from higher latitudes, just prior to an initiation of the MJO, and in turn, they propagate back toward the higher latitudes from the MJO active region over the Indian Ocean. A three-dimensional regression reveals an equivalent barotropic structure of the MJO vortex pair with the signs opposite to those at 150 hPa underneath. A vertical normal mode analysis finds that this vertical structure is dominated by the equivalent height of about 10 km.

1. Introduction

The tropical atmospheric Madden–Julian oscillation (MJO) is an eastward-propagating wavelike entity associated with strong convective activity (Zhang 2005). For this reason, the MJO is often considered an equatorial wave strongly coupled with convection (e.g., Emanuel 1987; Yano and Emanuel 1991; Fuchs and Raymond 2007; Raymond and Fuchs 2007, 2009; Majda and Stechmann 2009). Recently, Yano and Tribbia (2017) proposed an alternative theory that explains the MJO as a strongly nonlinear free solitary Rossby wave (see also Rostami and Zeitlin 2019). The basic premise behind this alternative theory is that the MJO dynamics is dominated by the vorticity field, and thus, a contribution of convection may be neglected to the leading order.

A perspective of the vorticity-dominated dynamics of the large-scale tropical circulation is originally suggested by Charney (1963). He suggested it by a scale analysis that the large-scale tropical circulation is nondivergent to the leading order (see also Yano and Bonazzola 2009). Observational data analyses (Yano et al. 2009; Adames et al. 2014; Žagar and Franzke 2015) support

Denotes content that is immediately available upon publication as open access.

Corresponding author: Jun-Ichi Yano, jiy.gfder@gmail.com

DOI: 10.1175/JAS-D-18-0172.1

this view. It naturally follows that the MJO may also be understood in terms of the vortex dynamics.

The role of the vorticity field, especially a dipolar-vortex structure, associated with the MJO is already long recognized in various previous observational data analysis (e.g., Knutson and Weickmann 1987; Rui and Wang 1990; Hendon and Salby 1994; Matthews 2000; Yanai et al. 2000; Kiladis et al. 2005; Adames et al. 2014; Žagar and Franzke 2015). However, a main problem with those earlier observational studies is that the MJO is identified in reference to the large-scale convective activity, as approximately represented by the outgoing longwave radiation (OLR). The goal of the present study is to identify the MJO in the vorticity field from a point of view of the vorticity dominance of the tropical large-scale circulation, and compare the identified features herein with those by convection-based traditional methods.

A problem with the traditional convection-based identification method is that the vorticity field associated with the MJO tends to be too elongated in longitude (e.g., Fig. 2 in Kiladis et al. 2005) compared to the theoretical prediction by Yano and Tribbia (2017). The latter is about 3000 km, whereas the observationally identified scale tends to be a few times larger. Yano and Tribbia (2017) speculated that this discrepancy is because convection (OLR) is taken as a reference variable rather than the vorticity itself. It is most likely that the convection and the vorticity fields associated with the MJO are not perfectly in phase, but the latter fluctuates in phase relatively to the former. Thus, taking the convection field as a reference for the identification of the MJO leads to a smoothing effect to the vorticity field. A primary motivation of the present study is to verify this speculation.

The correspondence of the identified intraseasonal-scale eastward-propagating feature in the vorticity field over the Indian Ocean and the western Pacific with the MJO identified by conventional methods is verified by taking the regression against the OLR to see that the extracted vorticity-field evolution is indeed closely associated with the convective variability. Identification of the MJO in the vorticity field inevitably leads to an interpretation of the MJO in terms of the Rossby wave dynamics. This perspective further leads us to investigate a link between the MJO and the Rossby wave trains crossing a subtropical zone. The link of the MJO to the higher-latitude variability was initially suggested by Weickmann et al. (1985) and Knutson and Weickmann (1987). Gustafson and Weare (2004), Ray and Zhang (2010), and Ray and Li (2013) speculated from modeling studies that the Rossby wave train arriving from the higher latitudes (Northern Hemisphere) to the Indian Ocean "triggers" the MJO. Observational analyses by Hsu et al. (1990) and Zhao et al. (2013) support this speculation. Observational analyses by Murakami (1987, 1988), Hsu et al. (1990), Kiladis and Weickmann (1992), and Adames and Wallace (2014) further suggest that the Rossby waves are emanated from the MJO over the western Pacific. The present study is going to depict these likely processes in a more explicit manner by focusing on the analysis on the vorticity field.

Another important question left unanswered in respect to the theory of Yano and Tribbia (2017) is the dominant equivalent height associated with the MJO vorticity field. The theory finds that this parameter has a major influence on the preferred propagation speed: as the equivalent depth is decreased from 10 to 1 km, the preferred phase velocity and horizontal scale decrease from 8–18 m s^{-1} and 3000 km to 2–4 m s^{-1} and 2000 km. Observational studies already suggest that the dynamical fields associated with the MJO exhibits an equivalent barotropic vertical structure. Nishi (1989) emphasizes an equivalent barotropic nature of the intraseasonal variabilities in general. This feature is more explicitly seen for the MJO in, for example, Fig. 2 of Yano et al. (2009), Figs. 6–8 of Holloway et al. (2013), Fig. 8a of Zhang and Ling (2012), and Fig. 2 of Žagar and Franzke (2015). These studies suggest that the signals associated with the MJO have a single sign in the vertical direction throughout the troposphere with an opposite sign at the tropopause level, a typical structure of the equivalent barotropic mode. In this study, the equivalent height of the MJO is directly diagnosed by a vertical normal mode analysis by following Kasahara and Puri (1981) and Fulton and Schubert (1985).

The paper is organized as follows. The next section describes data used as well as the analysis methodology; the results are presented in section 3, and they are discussed and summarized in section 4.

2. Analysis methodology

a. Data

The present study focuses on the vorticity field by following a theoretical proposal by Yano and Tribbia (2017) that the MJO is a strongly nonlinear free solitary Rossby wave. The vorticity data are taken from the European Centre for Medium-Range Weather Forecasts (ECMWF) interim reanalysis (ERA-Interim; Dee et al. 2011). The data span from 1 January 1979 to 31 December 2016 with the resolutions of a day, 2.5° in longitude and latitude, and 24 vertical pressure levels from 1000 to 50 hPa. We take the 150-hPa pressure level in the most part of the following analyses, because a direct visual inspection often shows a well-defined dipolar-vortex structure associated with the MJO, as shown in, for example, Fig. 1 of

Yano and Tribbia (2017), at this level. The OLR from the National Oceanic and Atmospheric Administration (Liebmann and Smith 1996) is used as a representation of deep convection for the same period and with the same temporal and spatial resolutions. The climatological temperature profile in the vertical normal mode analysis in section 3d is also taken from ERA-Interim data.

b. Filtering

The data time series is filtered by following Matthews (2000): the annual cycle and the three subharmonics are first removed. This is accomplished by setting the Fourier coefficients for the corresponding frequencies to zero. Data are then passed through a 20–200-day bandpass Lanczos filter with 241 weights.

c. EOF

For extracting the MJO, the EOF decomposition is applied to the filtered vorticity at the 150-hPa pressure level. To emphasize the equatorial signals in the analysis, the vorticity is divided by $\sin\lambda$, where λ is the latitude, anticipating that the magnitude of the vorticity is scaled by the Coriolis parameter as a function of the latitude. To avoid a singularity, the equatorial values are taken as the average over the two closest latitudinal data points, at 2.5°S and 2.5°N. In presenting the results, $\sin\lambda$ is applied back to the obtained EOF patterns so that the actual vorticity field is seen. The obtained EOF time series [the principal components (PCs)], PC_j ($j = 1, 2, \ldots$), are normalized by the condition

$$\frac{1}{T}\int_0^T \mathrm{PC}_j^2(t)\,dt = 1, \tag{1}$$

where T is the analysis period.

We focus on a particular EOF pair that represents an eastward-propagating MJO mode. The time evolution of the system approximated by a dominant EOF pair, say, ith and jth, may be examined by a vector $\mathbf{Z}$ defined by

$$\mathbf{Z}(t) = [\mathrm{PC}_i(t), \mathrm{PC}_j(t)], \tag{2}$$

where PC_i and PC_j are the ith and the jth PCs, respectively. This vector $\mathbf{Z}$ may furthermore be characterized by the amplitude $A(t)$ and the phase $\alpha(t)$ defined respectively by

$$A(t) = [\mathrm{PC}_i^2(t) + \mathrm{PC}_j^2(t)]^{1/2}, \tag{3a}$$

$$\alpha(t) = \tan^{-1}[\mathrm{PC}_j(t)/\mathrm{PC}_i(t)]. \tag{3b}$$

d. Regression analysis

A spatial pattern of any variable associated with a given PC is estimated by a regression analysis, which approximates a time series of any physical variable $\varphi(t)$ by

$$\varphi(t) \simeq \overline{\varphi} + \varphi'_j \mathrm{PC}_j(t). \tag{4}$$

Here, PC_j is the time series for the jth PC. The best fit to the above equation provides the time-averaged field $\overline{\varphi}$ and the fluctuation φ'_j of the given variable associated with this PC. If the vorticity at 150 hPa itself is used for the regression, φ'_j recovers the jth EOF pattern by definition. Regression may be performed separately for individual seasons: those are defined for the Northern Hemisphere as winter [December–February (DJF)], spring [March–May (MAM)], summer [June–August (JJA)], and autumn [September–November (SON)]. Regression can also be applied to the vorticity of a different vertical level for inferring the vertical structure of the variability (section 3d).

The regressed pair φ'_i and φ'_j can be used to reconstruct a typical evolution associated with this pair as a function of the phase α [Eq. (3b)] by

$$\varphi'_i \cos\alpha + \varphi'_j \sin\alpha. \tag{5}$$

By further adding a lag τ to the above regression method [Eq. (4)], we can infer the most likely subsequent and precedent evolution of an obtained EOF pattern:

$$\varphi(t) \simeq \overline{\varphi} + \varphi'_j(\tau)\mathrm{PC}_j(t-\tau). \tag{6}$$

As a result, $\varphi'_j(\tau)$ presents the most likely evolution of the variable φ preceding as well as following the maximum of the given PC.

In all the following regression analyses, the F test is applied, and only the values that are statistically significant at the 99% level are shown in the graphics.

e. Wave activity flux

Furthermore, to see the sense of the wave energy propagation, the wave activity flux defined by Takaya and Nakamura (2001) is superposed. Here, the perturbation streamfunction used for calculating the wave activity flux is either from EOF patterns or from lag-regressed vorticity fields, and the basic flow is based on either the climatology or the seasonal mean of the vorticity field.

3. Results

a. Local EOF analysis

The EOF analysis is first performed over a local domain spanning over the Eastern Hemisphere (0°–180°E)

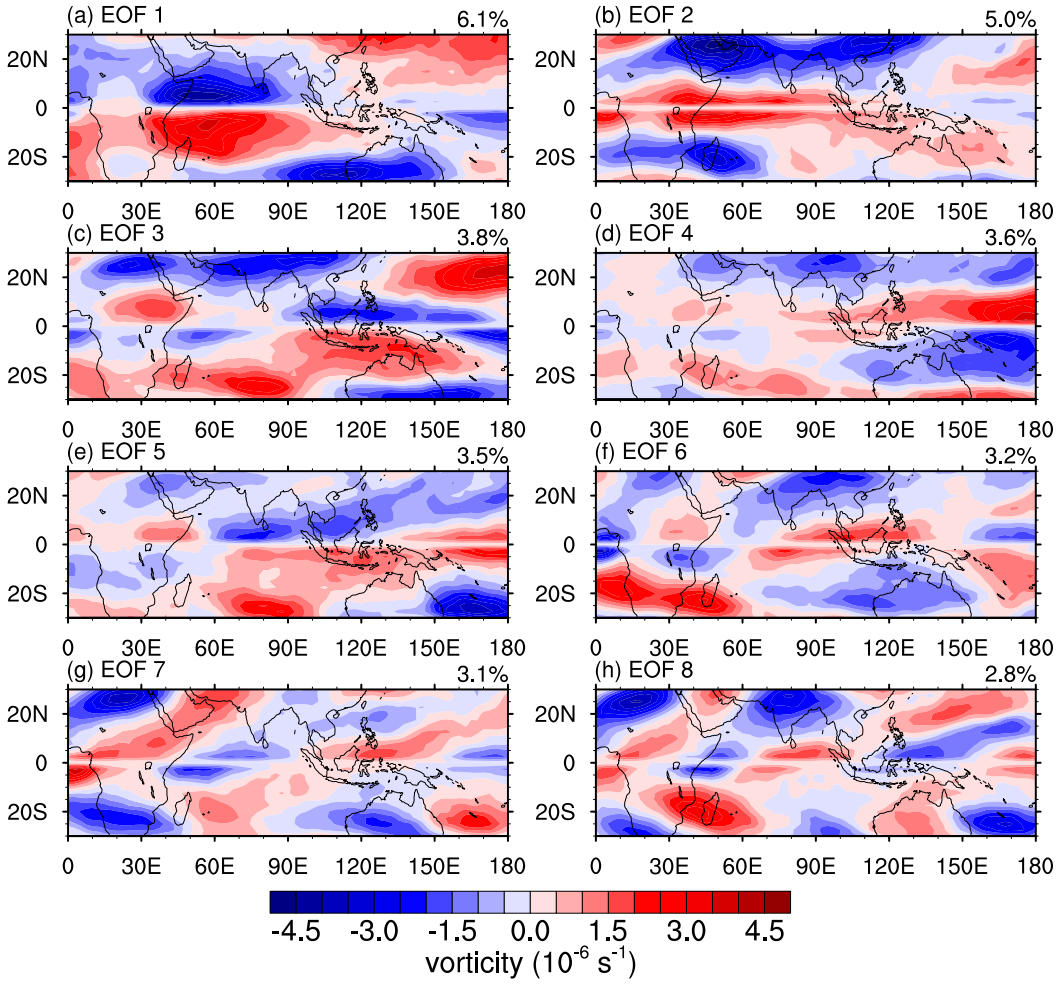

FIG. 1. The first eight EOFs of vorticity ($\times 10^{-6}\,s^{-1}$) obtained over the eastern tropics. The fractional contribution of each EOF is marked at the upper right of each panel.

and 30°S–30°N in latitude. Here, we focus on the Eastern Hemisphere, which covers both the Indian Ocean and the western Pacific, because over these regions, a slow eastward-propagating feature of the MJO, the main interest of the present study, is best identified: see further discussions in section 4b. When the EOF analysis was extended to the whole globe in longitude, the identified EOF modes were dominated by the variabilities over eastern Pacific to the Atlantic, not associated with the MJO in any obvious manner.

The obtained first eight EOFs are shown in Fig. 1. We focus on the first eight, because the signals become weaker near the equator and also become less symmetric about the equator for the higher EOFs. Dipolar structures, consisting of an anticyclonic vortex pair in both hemispheres, are identified from the Indian to the Pacific Oceans (in the order of being identified from west to east) in the first, fifth, third, and fourth EOF modes. These dipolar structures are reminiscent (albeit with the opposite sign) of the solitary Rossby vortex pair studied by Yano and Tribbia (2017), being trapped to the equatorial region (20°S–20°N).

The longitudinal scale in the first EOF is rather large, extended for 6000 km from 30° to 90°E; that of the third EOF is slightly smaller, extended for 4500 km from 90° to 135°E. Nevertheless, these scales tend to be closer than those of the earlier observational analyses to theoretically predicted scale of 3000 km by Yano and Tribbia (2017). Here, the first EOF accounts for 6.1% of the total variance for the vorticity divided by $\sin\lambda$. This value is comparable to that of the leading-order EOF identified for the OLR field by Matthews (2000) by a similar method (6.6%). On the other hand, when the filter width is narrowed to 30–70 days, fractional contributions of the first only increase to 7.0%. This is in contrast to the OLR-based analysis by Matthews (2000), in which the contribution doubles by narrowing the filter width in a similar manner.

For identifying a possible pair of EOFs that corresponds to a slow eastward propagation of the MJO, we infer the mutual time dependence of those EOF modes by the lag correlations: Fig. 2 shows the maximum (in absolute values) lag correlation coefficients (Fig. 2a) and the lag leading to the maximum for all the possible correlation combinations among the first eight EOFs (Fig. 2b). The lag correlations are evaluated for the range from −45 to 45 days. The lag is defined in such a manner that a positive value suggests that an EOF mode in the row leads that in the column. The lag correlation between the first and the third EOFs is found most distinguished among all the possible pairs with the maximum lag correlation of 0.24, whereas the lag correlations of the other pairs fall well below 0.2 in magnitudes. Thus, we decide to focus on this pair in the following.

The best lag between them, 9 days, suggests that the dipolar structure over the Indian Ocean (first EOF) precedes that over the western Pacific (third EOF) by 9 days. The obtained lag is comparable to those obtained with some indices proposed for the MJO: the all-season real-time multivariate MJO index (RMM; Wheeler and Hendon 2004), the velocity potential multivariate index (VPM; Ventrice et al. 2013), and the OLR-based MJO index (OMI; Kiladis et al. 2014) as shown in Table 1 of Adames and Wallace (2014).

To see details of the lag structure, the lag correlation between the first and the third EOFs is plotted as a function of the lag in Fig. 2c, in which we identify the three prominent peaks in the lag correlation: −46, −10, and 9 days. A lag of −10 days, with a negative correlation, suggests that the first EOF is minimum after 10 days when the third EOF is maximum; a lag of −46 days, with a positive correlation, suggests that the first EOF returns to the maximum 46 days after the maximum of the third EOF. Thus, a complete cycle is realized over the 46 days initiated with an eastward propagation of a dipolar structure from the Indian Ocean to the western Pacific.

Matthews (2000) performed a similar analysis with OLR, and identified MJO cycles for a period from December 1987 to April 1988. Figure 3a plots the time series of the two identified principle components from the vorticity field by our analysis for this period. An off-phase relation between these two principal components is well identified over the period from November 1987 to February 1988, in a similar manner as in Matthews (2000).

If the EOF pair identified in the vorticity field is indeed associated with the MJO, we also expect an enhanced convective activity associated with this pair. More specifically, we expect that convection is more active over the Indian Ocean and the western Pacific, respectively, when the first and the third EOFs are

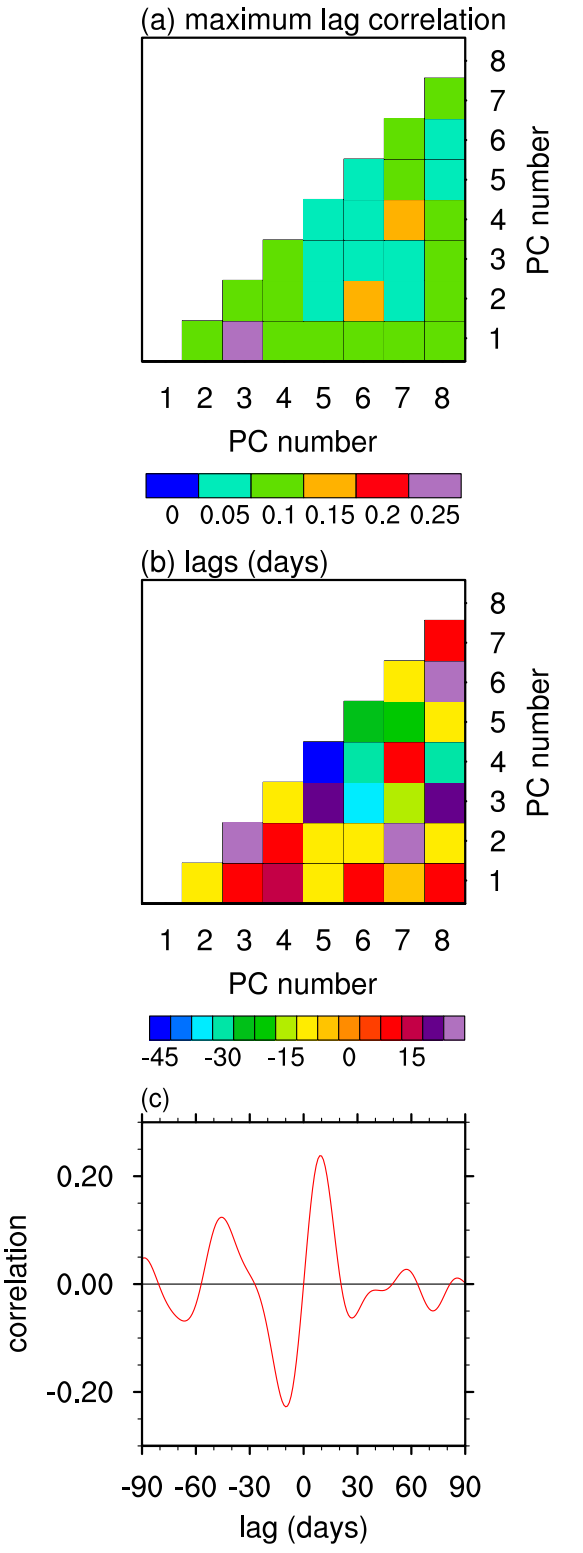

FIG. 2. (a) Maximum (absolute value) lag-correlation coefficients and (b) the corresponding lags (days) of the first eight PCs. The labels for rows and columns indicate the PC numbers. A positive lag means the PC in the row leads the PC in the column. (c) Lag correlation between the first and the third PCs as a function of the lag (days).

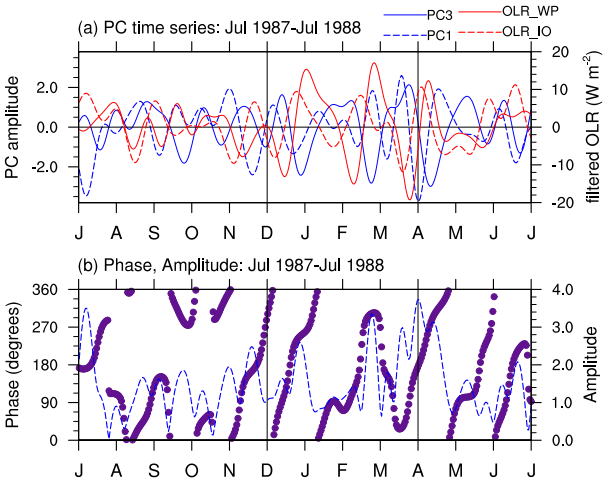

FIG. 3. (a) Time series of the first (blue dashed) and the third (blue solid) local PCs as well as the OLR time series averaged over the Indian Ocean (OLR_IO; red dashed) and the western Pacific (OLR_WP; red solid). (b) Phase $\alpha(t)$ (purple dotted) and amplitude $A(t)$ (blue dashed) of $\mathbf{Z}(t) = [\mathrm{PC}_1(t), \mathrm{PC}_3(t)]$ during July 1987–July 1988. The 4-month period marked by vertical black lines corresponds to the period of three MJO cycles identified by Matthews (2000). Here, the PCs are normalized by Eq. (1).

dominant. To verify this, the time-filtered OLR averaged over the Indian Ocean (30°S–30°N, 50°–120°E) and the western Pacific (30°S–30°N, 100°–150°E) are also plotted in Fig. 3a. PCs and these OLR time series are relatively well correlated with their maximums and minimums corresponding to each other reasonably. The correlation between the first EOF and the OLR averaged over the Indian Ocean and that between the third EOF and the OLR averaged over the western Pacific are −0.42 and −0.46, respectively. It suggests that the dipolar structure identified in the vorticity field is indeed associated with a local enhancement of convection.

The characteristics for PCs defined by Eqs. (3a) and (3b) are plotted for the identified EOF pair (i =1 and j = 3) in Fig. 3b for the same period as in Fig. 3a. The eastward propagation is suggested more clearly in the phase time series here. Four cycles of eastward propagation identified over the period from November 1987 to June 1988 are in agreement with Fig. 2d of Matthews (2000): two complete cycles over November 1987–January 1988 and another two over March–June 1988 with a break between these two periods. A further eastward-propagating event is also identified over January–February 1988. However, this cycle is never completed. The amplitude $A(t)$ does not represent an obvious correlation between the active phase of the MJO over the Indian Ocean (α = 0°) or the suppressed phase (α = 180°), although it may be notable that the amplitude is largest during the third MJO cycle over March–April 1988.

A typical spatial evolution associated with the PC pair (first and third) can be inferred from a linear combination of these two EOF modes with a weighting modified with the evolution of the phase α by setting φ_1' and φ_3' to EOF_1 and EOF_3 in Eq. (5). The result in Figs. 4a–e for the phases α = 0°–90° shows that the eastward propagation of the vortex pair from the Indian Ocean to the western Pacific is not quite continuous, but rather consists of a jump of the vortex pair from a region to another with a relatively weak elongated vortex pair seen at a transition phrase (α = 45°).

The associated evolution of the OLR field is obtained by the regression setting φ' = OLR in Eq. (4), and then setting φ' = OLR in Eq. (5) with the selected phases α (Figs. 4f–j). The associated eastward propagation of OLR is more continuous in time than that of the vorticity field. The plot is reminiscence of Fig. 3 of Matthews (2000), which is obtained by a direct application of EOF to OLR. The correspondence demonstrates that the EOF pair identified in the vorticity field indeed represents the MJO.

b. Global EOF analysis

The same analysis as the last subsection is repeated globally for examining possible interactions of the MJO with the extratropical Rossby waves, as speculated by Gustafson and Weare (2004), Ray and Zhang (2010), Ray and Li (2013), and Zhao et al. (2013). The EOF modes depicted by the local analysis in the last subsection already suggest that the vorticity variability associated with the MJO is not well confined to the equatorial region, but further extends to the higher latitudes.

The global EOF analysis is performed also by dividing the vorticity at 150 hPa by sinλ to obtain the variabilities preferably centered to the equator. Nevertheless, as it turns out, more or less all the identified EOF patterns represent global characteristics, making it difficult to identify MJO modes among them in a straightforward manner. Temporal correlations of these global PCs with the first and the third local PCs are taken to identify the MJO modes from these global EOFs. The results for the first 30 global EOF modes are shown in Fig. 5. The correlations with the higher global EOF modes are much weaker.

The strongest correlation with the first local PC is found with the seventh global PC. Its spatial pattern (Fig. 6a) represents a similar dipolar vortex over the Indian Ocean. The first local PC is also well correlated with the twelfth and the thirteenth global PCs. The corresponding two global EOF modes represent meridional wavelike patterns crossing the tropical Indian Ocean with the peaks over the Arabian Peninsula and China, respectively. These patterns suggest interactions between the MJO over the Indian Ocean and signals

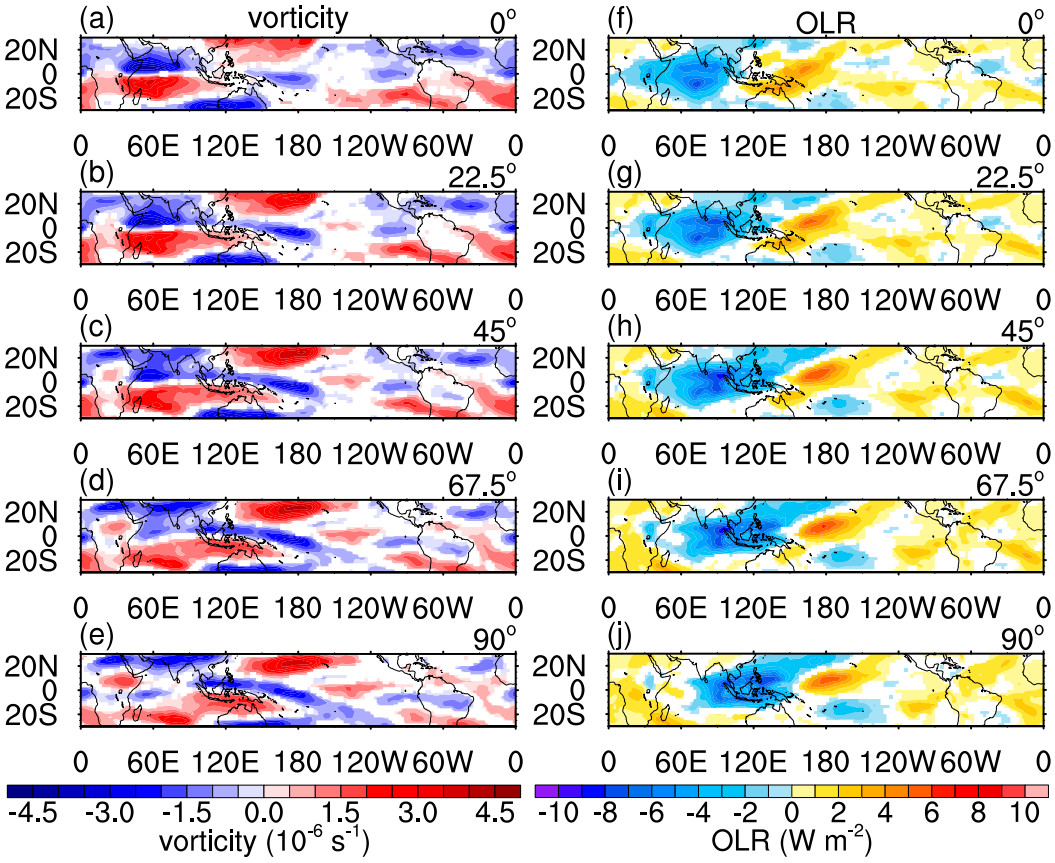

FIG. 4. The regression maps of (a)–(e) the vorticity ($\times 10^{-6}$ s^{-1}) and (f)–(j) the OLR (W m^{-2}). The phase (°) is marked at the upper right of each panel. Only the values above the 99% significance level are shown.

from the higher latitudes. The first local PC is also correlated with some other global PCs (first, third, fourth, fifth, eighth, ninth, and eleventh). However, the corresponding EOF patterns are characterized by more variabilities over the eastern Pacific and the Atlantic. Notably the global fourth and the eleventh EOFs contain equatorial dipolar vortex over the date line.

A closer look of the seventh global EOF in Fig. 6a reveals several extratropical signals. First noted is a dipolar vortex located in the northern central Pacific with anticyclonic vorticity in the north. A similar feature is also identified by, for example, Weickmann et al. (1985; see their Fig. 9a) in association with the MJO. It most likely corresponds to blocking, as it is climatologically known that it is dominant over this area along with the North Atlantic [cf. Fig. 2 of Dole and Gordon (1983) and Fig. 8 of Small et al. (2014)]. Typical composites of the North Pacific blocking state [e.g., Figs. 7 and 16 of Small et al. (2014)] are shifted slightly northward, but otherwise the structure is very similar.

The second most noticeable feature is a Rossby wave train crossing over the tropical Atlantic meridionally: it stretches northward to 30°N, and the feature can be traced southward for a substantial distance, crossing South America, and reaches the southeastern Pacific. Crossing the southern Pacific, it turns back northward over the southwestern Pacific toward the Indian Ocean, although gradually weakening in signal by tracing backward. This feature can be interpreted as a Rossby wave train following a trajectory along a great circle connecting the Indian Ocean and the tropical Atlantic (cf. Hoskins and Karoly 1981).

A superposed wave activity flux (section 2e) converges toward the equator over the Atlantic. Over the Indian Ocean, a southward energy flux is identified over the Southern Hemisphere positive anomaly. The magnitude of the wave energy flux in between is rather weak. Nevertheless, it is possible to trace the northeastward flux backward from the Atlantic Ocean to the South Pacific.

Figure 5 shows that the third local PC is correlated well with the fourth, fifth, and eighth global PCs, with the highest correlation with the fourth. The eighth global EOF contains a similar dipolar structure as the

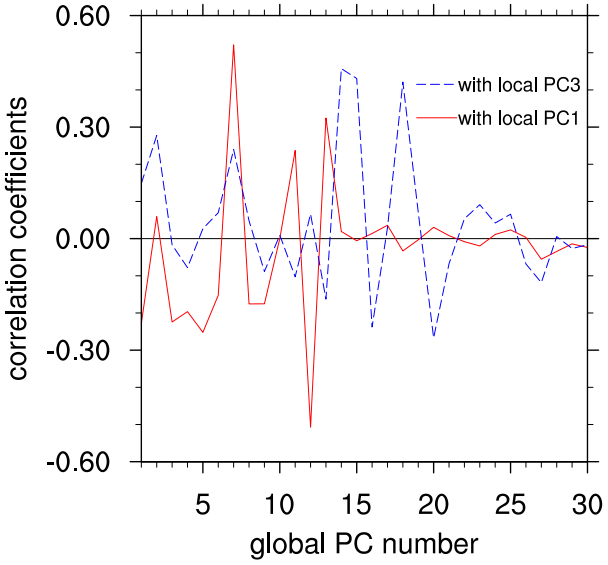

FIG. 5. The correlation coefficients of the first (red solid) and third (blue dashed) local PCs with the first 30 global PCs.

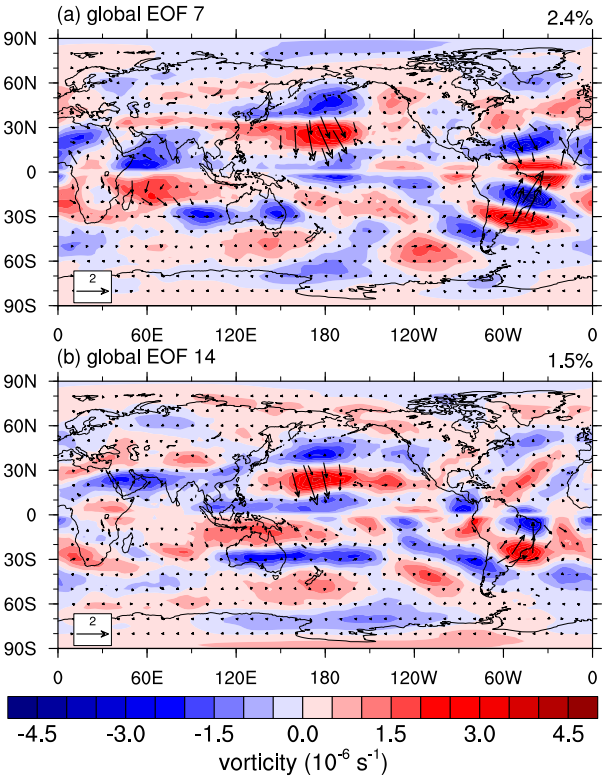

FIG. 6. The (a) seventh and (b) fourth global EOFs patterns ($\times 10^{-6}$ s^{-1}), representing the highest correlations with the two locally identified MJO modes—the first and third, respectively. The fractional contribution of each EOF is marked at the upper right of each panel. Superposed are wave activity flux vectors (m^2 s^{-2}) with the reference vector shown in the lower left of each panel.

third local EOF over the western Pacific. The third local PC is also significantly correlated with the second, seventh, sixth, and twentieth global PCs. Recall that the seventh global PC is the best correlated with the first local PC.

The fourth global EOF pattern is shown in Fig. 6b. As in the case with the seventh global EOF, the dipolar vortex over the northern Pacific is prominent. As a major difference from the seventh EOF, this dipolar vorticity is no longer well isolated, but it appears to constitute a part of the Rossby wave train crossing the equatorial western Pacific with a southern counterpart dipolar vortex identified over Australia; the MJO vortex pair is identified right at the equator along this Rossby wave train structure. The four of these vortices centered around the equator are reminiscent of a structure identified by Adames and Wallace (2014).

c. *Evolution of the 150-hPa MJO vortex pair*

The global evolution of the vorticity field in association with the MJO vortex pair may be inferred by two different approaches. A first possibility may be to identify a series of pairs of global EOFs by lag correlations in a similar manner as an eastward propagation is identified by a pair of local EOFs in section 3a. However a preliminary attempt along this line turned out to be rather involved, because almost every global EOF mode is highly lag correlated with multiple global EOF modes. It suggests that the global system associated with the MJO vortex pair can evolve into multiple directions rather than a single well-defined evolution tendency.

As an alternative, a more direct approach is taken, in which the lag-regression analysis is performed on the global vorticity field against the local PC pair identified as an MJO signal in section 3a by following the methodology described in section 2d. The results of the lag regression against the first and third local PCs are shown in Figs. 7 and 8, respectively. The lag regression elucidates two major processes associated with the MJO vortex pair: (i) its eastward propagation and (ii) its interaction with subtropical Rossby wave trains. These aspects are discussed in order. The regression is also performed separately for different seasons to examine seasonality. For tracing the propagation of the Rossby wave energy, the wave activity flux (section 2e) is also superposed on those regression maps.

1) EASTWARD PROPAGATION

Over an initiation phase, the cyclonic pair is gradually replaced over the Indian Ocean by an anticyclonic pair as seen in the regression against the first local PC (Figs. 7a–d). Once the MJO vortex pair is locally established, it begins to propagate eastward. Unfortunately, a

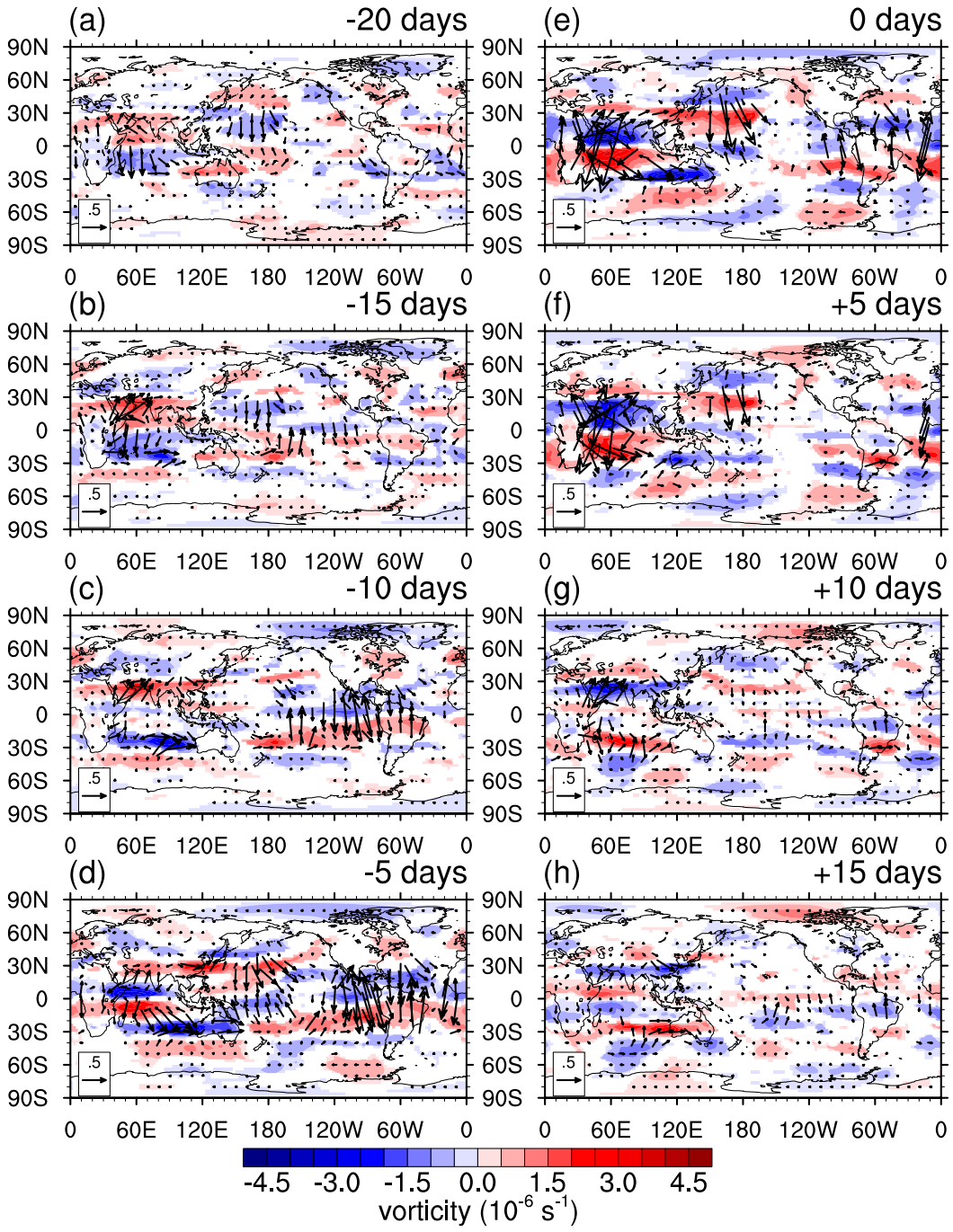

FIG. 7. Lag-regression maps of the vorticity ($\times 10^{-6}\,s^{-1}$) against the first local PC at lags (a)−20 to (h) 15 days with a 5-day interval. The lag (days) is marked at the upper right of each panel. Here, only the values above the 99% confidence level are shown. Wave activity flux vectors ($m^2\,s^{-2}$) are further superposed, as in Fig. 6.

direct inspection of the regression maps with the first local PC (Figs. 7e,f) does not reveal this tendency clear enough. This tendency is slightly clearer with the regression against the third local PC (Figs. 8b–d), but not much better.

For depicting the eastward propagation of the MJO vortex pair better, Fig. 9 presents the two time–longitude sections based on lag regressions of the global vorticity field against the first and the third local PCs. The regressed vorticity field is averaged over 15°S–15°N, flipping the sign for the values in the Southern Hemisphere. The regression against the first local PC in Fig. 9a shows that the vortex pair over the Indian Ocean (centered

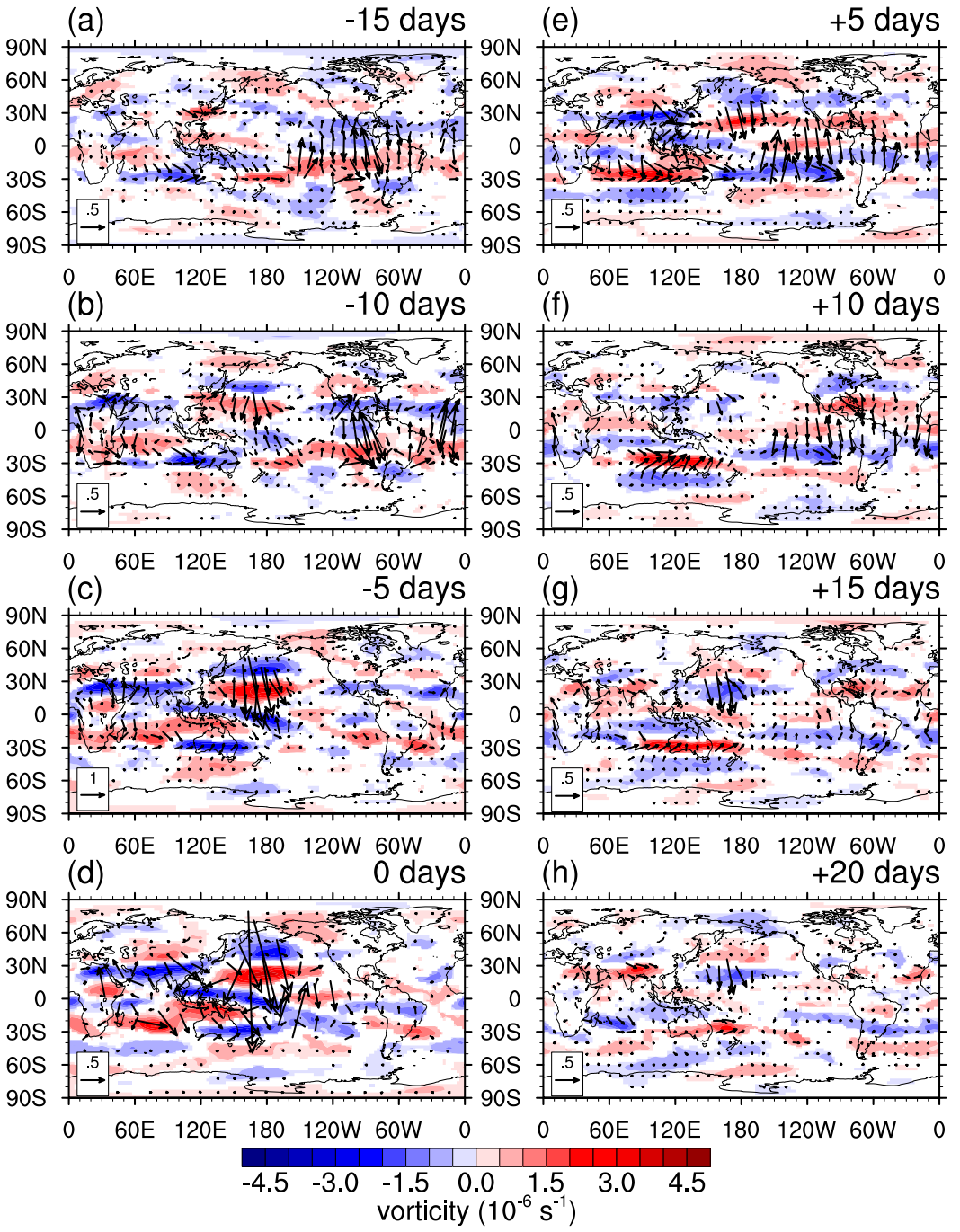

FIG. 8. As in Fig. 7, but against the third local PC from lags (a) −15 to (h) 20 days.

around 60°E), marked by a negative anomaly, tends to propagate eastward albeit in association with a drastic decrease of its amplitude after 10 days. The regression against the third local PC in Fig. 9b depicts the eastward-propagation tendency of the vortex pair clearer than the regression against the first PC. However, an overall amplitude of the variability associated with the third local PC is relatively weak: the scale range used in Fig. 9b is half of that in Fig. 9a. In this case, the vortex-pair amplitude enhances as it propagates from the Indian Ocean to the western Pacific, though the signal decreases after crossing the date line.

The eastward propagation of the vortex pair has different features in different seasons (Fig. 10). The eastward

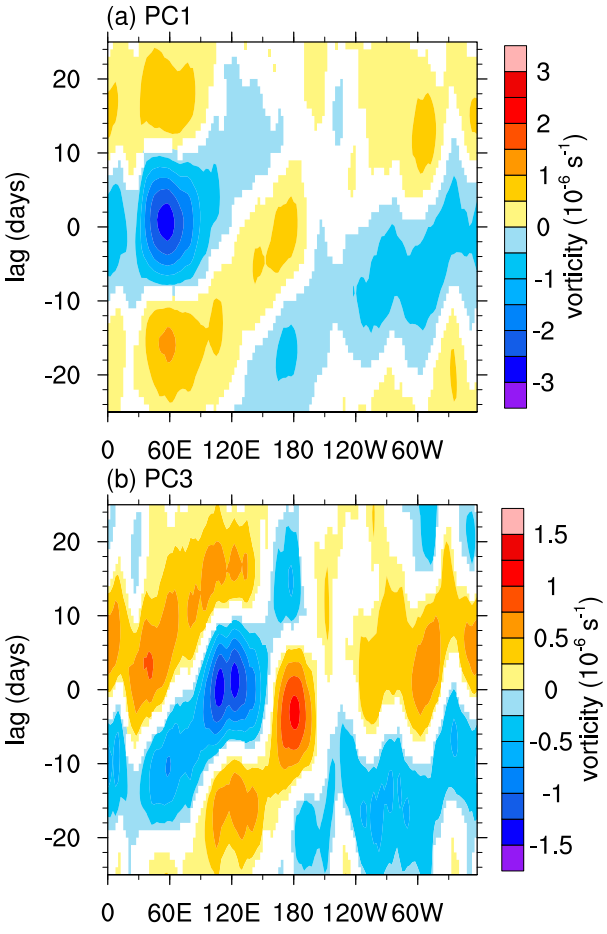

FIG. 9. Time–longitude sections of the lag-regressed vorticity ($\times 10^{-6}$ s^{-1}) against the local (a) first and (b) third PCs. The regressed vorticity is averaged between 15°S and 15°N with the sign flipped for the Southern Hemisphere. Only values above the 99% confidence level are shown.

propagation is most extended longitudinally in DJF (Fig. 10a): the propagation begins at 60°E and ends near 150°W in a continuous manner and with a large amplitude. The eastward propagation is fastest from the Indian Ocean to the western Pacific in MAM (Fig. 10b), but the propagation is terminated at 150°E. The cycle is also the shortest in MAM. The eastward propagation in SON (Fig. 10d) is overall similar to that in MAM, but is slightly slower. In JJA (Fig. 10c), no eastward propagation from the Indian Ocean to the western Pacific is seen, but a signal propagates westward from the Indian Ocean. On the other hand, the eastward propagation over the Pacific is most distinguished among the four seasons. This is somehow consistent with Fig. 3 of Zhang and Dong (2004), in which the spectral power of the MJO-related low-level zonal wind and precipitation is strongest over 120°–150°E in JJA.

A failure to capture an eastward propagation in JJA reflects a lack of MJO signal over the Indian Ocean in this season (cf. Salby and Hendon 1994). It is well known that the tropical intraseasonal variability during the Northern Hemisphere summer over the Indian Ocean is dominated by a northward-propagating mode. In earlier studies this mode is referred to as Yasunari waves (Yasunari 1979, 1980, 1981). Jiang et al. (2004) retermed this mode as boreal summer intraseasonal variability (BSISO). We have verified that indeed the vorticity field also propagates northward associated with convective variability in JJA.

2) Interaction with Rossby wave trains in higher latitudes

It has been speculated (Gustafson and Weare 2004; Ray and Zhang 2010; Ray and Li 2013) that the arrival of Rossby wave trains from higher latitudes to the Indian Ocean triggers an MJO. For delineating this process, the time–latitude sections from the same regressions are presented in the following. Here, the longitudinal range for the time–latitude sections are shifted with latitude by closely following the tendency of the Rossby wave trains propagating eastward as they propagate latitudinally. Note that the Rossby wave train transports the energy, and we trace this process by following an evolution of a high-amplitude region, albeit its sign may change over energy propagation.

Figure 11 shows time–latitude sections of regressions against the first local PC constructed over the Indian Ocean. The tilted longitudinal band marked by the two red lines in Fig. 11a is adopted by following the southward propagation of Rossby wave trains as seen in Fig. 6a. For the whole year (Fig. 11b), equatorward propagation of Rossby wave trains from higher latitudes to the Indian Ocean before the active phase of the MJO is suggested by the high wave activity centered at 25°N with a positive anomaly with a lag of −15 days. This tendency is most prominent in DJF (Fig. 11c) and to a lesser extent in MAM (Fig. 11d). The equatorward propagation of wave activity from higher latitudes to the Indian Ocean is less evident in JJA (Fig. 11e) and SON (Fig. 11f). Figure 11 further suggests that the positive vorticity anomaly originally identified at 25°N with a lag of −15 days continues to propagate southward by crossing the equator. This tendency is already evident for both the whole year (Fig. 11b) as well as in DJF (Fig. 11c), but most prominent during MAM (Fig. 11d). In this manner, these section plots suggest that a Rossby wave train arrives at the Indian Ocean from a European region.

Although much less clear than the time–latitude sections (Fig. 11), lagged snapshots by regression against the first PC (Fig. 12) may trace the evolution of the vorticity field associated with the latitudinal Rossby

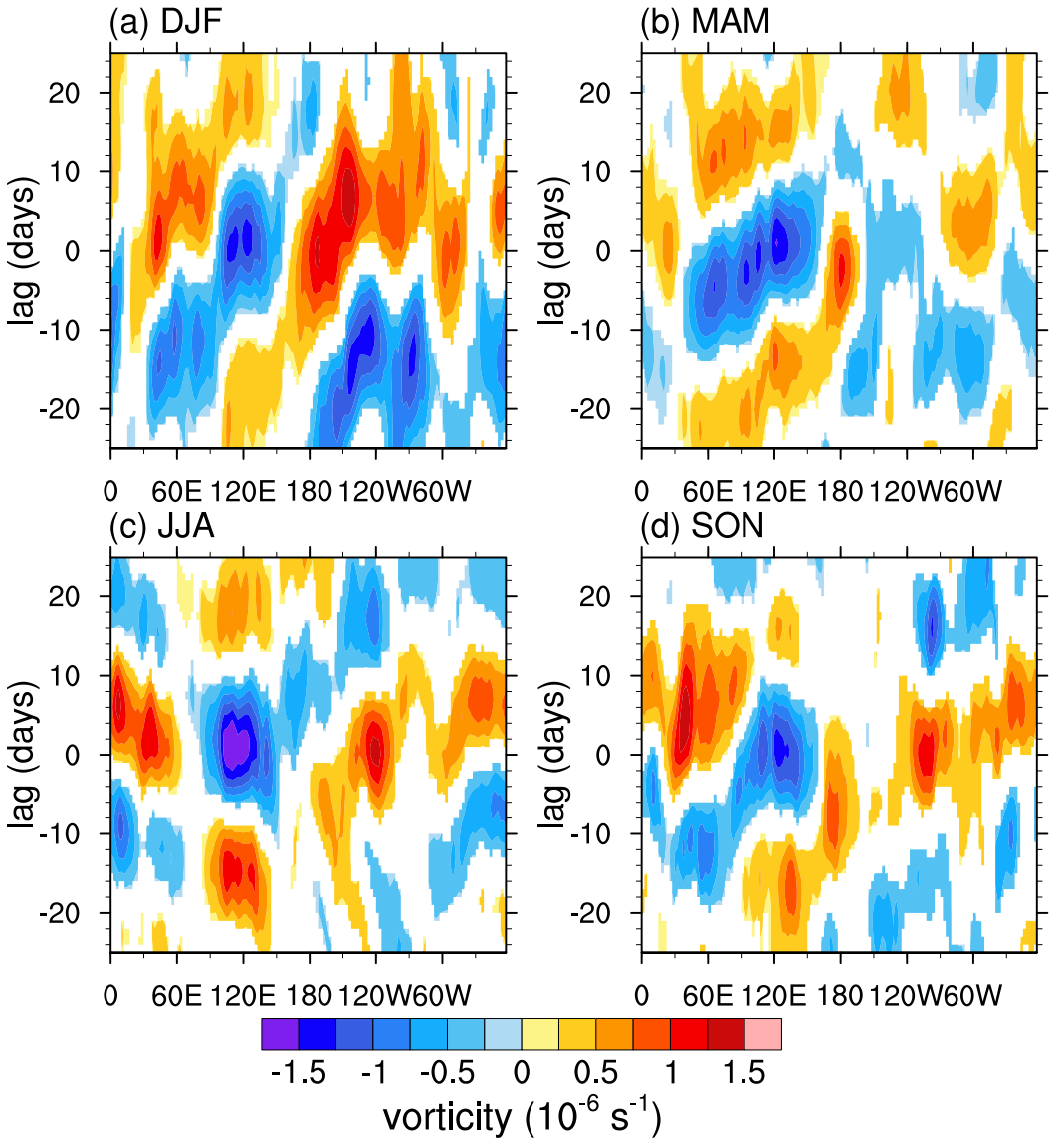

FIG. 10. Time–longitude sections of the lag-regressed vorticity ($\times 10^{-6}$ s^{-1}) against the third local PC for the four seasons: (a) DJF, (b) MAM, (c) JJA, and (d) SON. The regressed vorticity is averaged between 15°S and 15°N with the sign flipped for the Southern Hemisphere. Only values above the 99% confidence level are shown.

wave train propagation: the beginning of its equatorward propagation may be identified by a negative anomaly centered around 45°N, 20°E with a lag of −20 days (Fig. 12a). The wave amplifies as its energy propagates southeastward (but changing the sign of the vorticity). The highest energy amplitude is identified at 20°N, 50°E with a lag of −12 days (Fig. 12b), and the center of the wave activity moves to the right at the equator, as identified by a well-defined equatorially trapped vortex pair, with a lag of −6 days (Fig. 12c), corresponding to an MJO.

The southward energy propagation of the Rossby wave activity is further quantified by superposing the wave activity flux (section 2e). Expected southward energy flux associated with the southward propagation of the Rossby wave train is relatively weak. Nevertheless, a southward wave activity flux over 20°–30°E at 30°N at the lag −20 days in DJF (Fig. 12a) suggests wave energy propagation from a European area farther north. This flux appears to enhance the positive anomaly centered to 20°N, 30°E at the lag −12 days. From there, the energy propagation brunches out to the east along the westerly jet (cf. Fig. 13a), and to the south along East Africa. The latter appears to further induce a negative vorticity anomaly to the equator at the lag −6 days, which finally constitutes a part of the MJO vortex pair that propagates eastward.

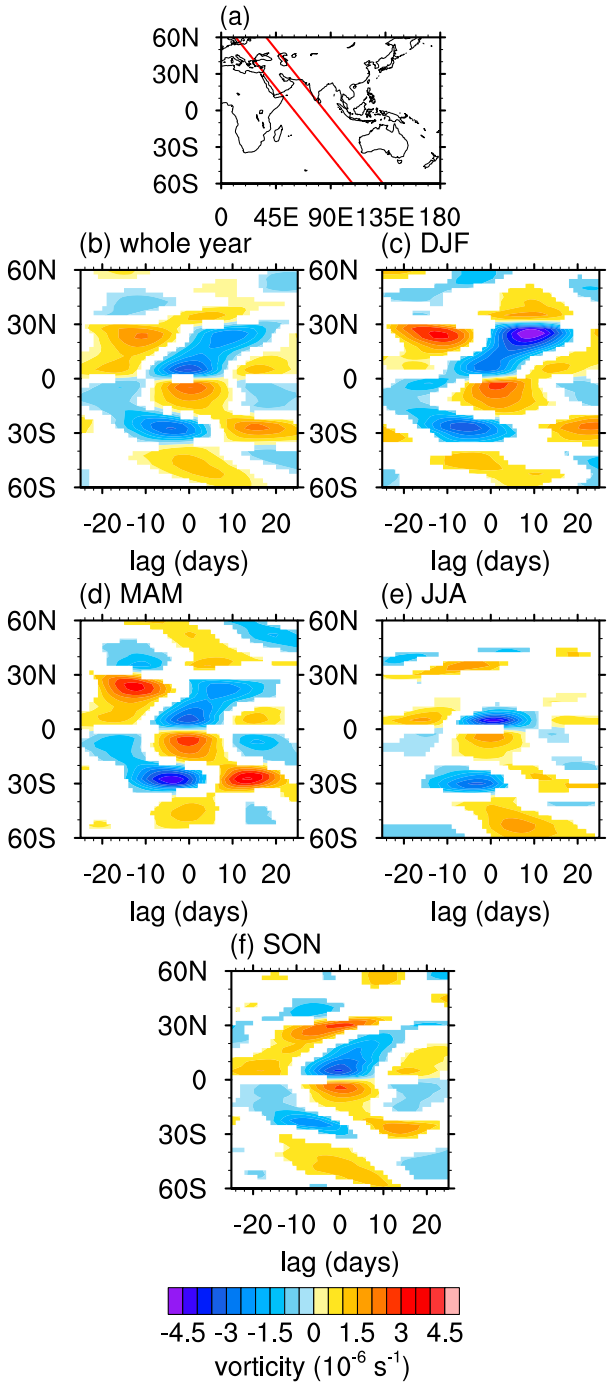

FIG. 11. Slanted time–latitude sections of the lag-regressed vorticity ($\times 10^{-6}$ s^{-1}) against the first local PC. (a) The longitude range is marked by the red lines. The regression is for (b) the whole year, (c) DJF, (d) MAM, (e) JJA, and (f) SON. Only values above the 99% confidence level are shown.

Prior to the maximum phase of the MJO vortex pair over the Indian Ocean in DJF (Figs. 12a–c), the most noticeable is eastward wave activity flux along 20°N, which moves the positive vorticity anomaly centered around 30°–90°E at the lag −20 days eastward with time, and the same anomaly is found over the northern Pacific at the lag 0 days. A negative anomaly to the north in the pair also follows this propagation tendency, although the energy flux tendency is less clear for this northern counterpart. The eastward propagation of the wave energy identified here can be attributed to a strong westerly jet dominated over this region during DJF, as seen in Fig. 13a. This interpretation is supported by the fact that the eastward wave activity flux is no longer seen when the contribution of the background zonal wind is excluded in its evaluation.

As the MJO vortex pair established over the Indian Ocean at the lag −6 days, the southward energy flux begins to enhance and to cross the equator (Figs. 12d–f). At the same time, the poleward energy flux to its east side (60°–90°E) is also noted, contributing to poleward expansion of this vortex pair with time (Figs. 12d,e). The northward energy flux from the negative vorticity anomaly associated with the MJO vortex pair appears to contribute to an enhancement of a positive anomaly immediately north over central Asia. On the other hand, the southern counterpart of the MJO vortex pair somehow begins to weaken after the lag +3 days. As a result, a vortex pair in the Northern Hemisphere over central Asia is identified at the lag +9 days (Fig. 12f) in place of the original MJO vortex pair. The northward energy flux associated with the central Asian vortex pair appears to further enhance an already established vortex pair over the northern Pacific (Figs. 12d,e).

A similar process is also found during MAM (Fig. 14), but with some differences. Wave activities arriving at the Indian Ocean from the north are weaker. Formation of the wave train crossing the equator farther southward is equally noticed. Establishment of the vortex pair over the northern Pacific is equally remarked, although its formation process appears to be more involved. The eastward propagation of energy along the positive anomaly along 20° at lags −20 to −14 days still stands out, and it is again attributed to a strong westerly jet over this area (Fig. 13b). Though the signals are even weaker, we note a similar tendency in the regression for the whole year in Fig. 7.

The behavior of the MJO vortex pair over the Pacific Ocean is examined by slanted time–latitude sections of the regression against the third local PC (Fig. 15). Here, the longitudinal range for the analysis is marked by the two red lines as functions of latitude in Fig. 15a. The slant is defined in such a manner that the high-vorticity activities seen over the tropical western Pacific to the northern Pacific (cf. Fig. 6b) are covered well over the analysis domain. Sections are taken for the whole year (Fig. 15b), as well as for the four seasons separately

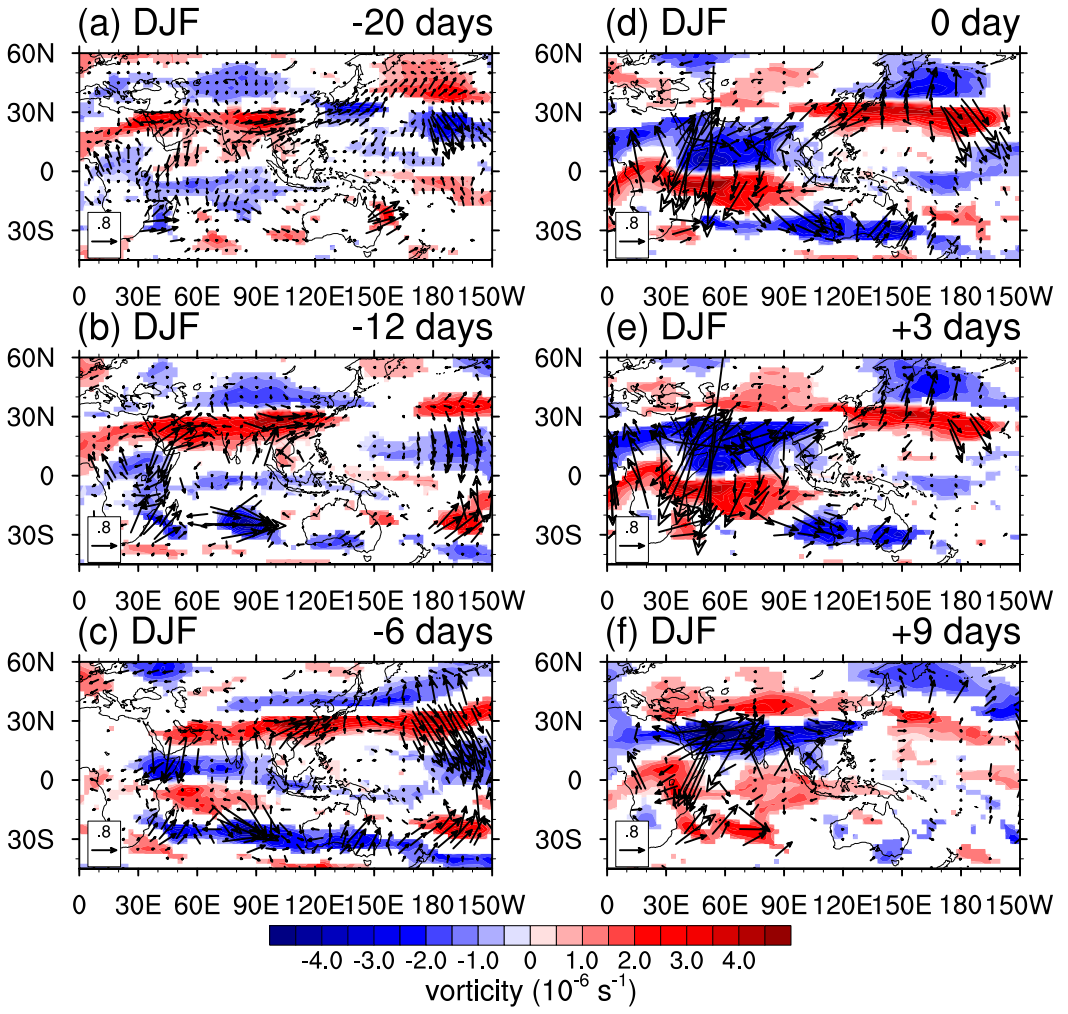

FIG. 12. Lag-regression maps of vorticity ($\times 10^{-6}\,s^{-1}$) against the first local PC for DJF. The lag (days) is marked at the upper right of each panel. Values are shown only if the regression is statistically significant at the 99% level. The wave activity flux vectors ($m^2\,s^{-2}$) are superposed, with the reference vector shown in the lower left of each panel.

(Figs. 15c–f). Unlike the analysis over the Indian Ocean, the slanted time–latitude sections over the Pacific Ocean does not represent any clear sign of the latitudinal propagation of the wave activities. Rather, a vortex-train structure over the Pacific, already identified in Fig. 6b, is simultaneously generated over the latitudinal band from 40°S to 50°N. This tendency is most evident for the whole year (Fig. 15a) as well as for MAM (Fig. 15d). In DJF (Fig. 15c) and JJA (Fig. 15e), though we notice some propagation tendencies, it is hard to interpret with mixtures of the tendencies for both northward and southward propagations.

These latitudinal propagations of the Rossby wave activity, furthermore, appear to link the eastward propagation of the MJO vortex pair along the equator with the slow eastward-propagating Rossby waves in midlatitudes, as already remarked in examining Fig. 12. This tendency is more explicitly seen in time–longitude sections of the regression against the third local PC for the whole year as well as for separate seasons in Fig. 16. The regressed field is averaged over 20°–35°N in Figs. 16a–e: the vorticity signal with wavenumber 1 is circulating around the globe relatively continuously. The period is about 50 days both for the annual average and for DJF and MAM, whereas the propagation speed doubles for JJA and SON. The same plots are also repeated for the average over 20°–35°S (Fig. 16f–j): similar propagating features are identified as the Northern Hemisphere as an approximate mirror image, although these features are less obvious in direct inspections of the regressions maps. Note that these signals are relatively weak (the amplitude of $10^{-6}\,s^{-1}$) in the standard of the midlatitudes.

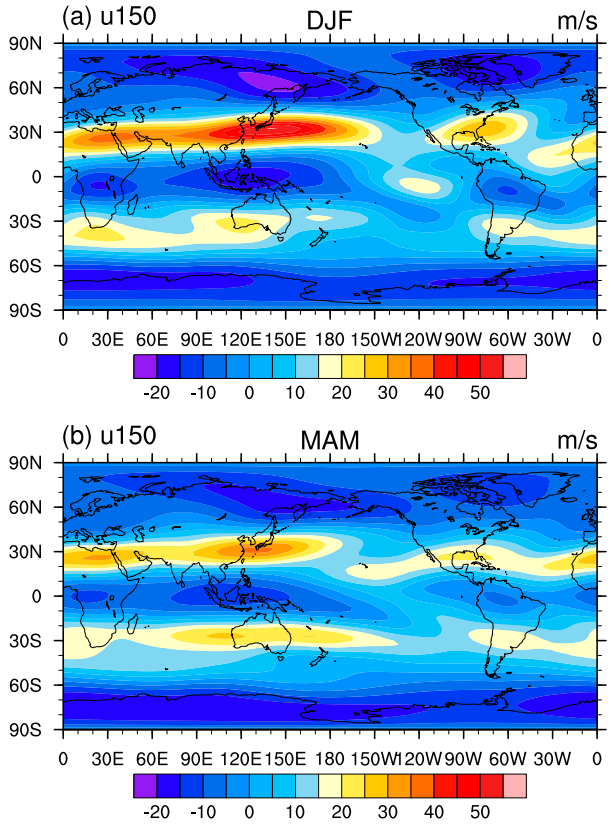

FIG. 13. The seasonally averaged climatological 150-hPa zonal wind ($m\,s^{-1}$) in (a) DJF and (b) MAM.

These waves are likely to correspond to a tail of the spectral signal of the planetary Rossby waves peaked at the 16-day period as identified by Madden (1978).

d. *Vertical structure*

Finally, we examine the vertical structure of the MJO vortex pair extracted by the local EOF analysis. For this purpose, the three-dimensional vorticity field is regressed against the first and the third local PCs [based on Eq. (4)]. The height–latitude section of the regressed vorticity field against the first PC at 55°E is shown in Fig. 17a and against the third PC at 130°E in Fig. 17b. As seen in both figures, these two EOF modes are confined to the upper troposphere over 80–300 hPa. Recall that the dipolar signal with the third EOF is weaker than that of the first EOF (cf. Fig. 1). This fact is also reflected upon the two vertical sections herein. The vortex pair over the Indian Ocean (Fig. 17a) changes the sign of the vorticity below 400 hPa. On the other hand, over the western Pacific (Fig. 17b), the vortex pair remains the same sign almost down to the surface.

The height–longitude sections of the regressed vorticity field averaged between 15°S and 15°N with first and third PCs, shown in Figs. 17c and 17d, respectively, represent westward tilts with height, with a stronger tilt for the vortex pair over the Indian Ocean (Fig. 17c). Under the regression against the third PC (Fig. 17d), a vertically homogeneous cyclonic pair is identified from the surface to 300 hPa, with about a 10-km depth. This structure is consistent with a potential vorticity (PV) field found by Zhang and Ling (2012, their Figs. 5 and 8): during an active phase of the MJO, the PV is cyclonic in the mid- and lower troposphere, but becomes anticyclonic with higher amplitudes in the upper troposphere. They also found that the upper-PV center is to the east of the lower-PV center, being consistent with our result here. A tropospheric cyclonic vortex pair identified here corresponds well to the modon solution in an equivalent barotropic system considered by Yano and Tribbia (2017, cf. their Figs. 2 and 4).

Evolution of this equivalent barotropic structure is further delineated by the height–longitude sections regressed against the third PC from lags −15 to 15 days (Fig. 18). With lag −15 days, before the active phase, the lower-troposphere western Pacific is dominated by anticyclonic vorticities. With lag −5 days, as the 150-hPa vortex pair propagates from the Indian Ocean to the western Pacific, the equivalent barotropic structure is formed over the Indian Ocean (60°–90°E), reaching the 300-hPa height. With lag +5 days, as the 150-hPa vortex pair arrives at the western Pacific, the equivalent barotropic structure is stretched upward and reaches the 200-hPa level at 90°E. With lag +15 days, the equivalent barotropic structure propagates farther eastward, as the 150-hPa vortex pair reaches the date line.

The 850-hPa vorticity field is also regressed against the third PC with lags −15 to +15 days (Fig. 19). With lag −15 days, an anticyclonic vortex pair is seen at 850 hPa over the western Pacific, as the cyclonic vortex pair is in a dry decaying phase at 150 hPa. As the 150-hPa anticyclonic vortex pair is formed over the Indian Ocean, the corresponding signal at 850 hPa is rather weak, but from lag −5 to +15 days, the 850-hPa-level cyclonic vortex pair gradually develops and propagates eastward from the Indian Ocean to the western Pacific. As a whole, the 850-hPa vortex pair is less organized and tends to be larger than the 150-hPa vortex pair.

An important parameter left undetermined in Yano and Tribbia (2017) is the equivalent height of the MJO vortex. Here, a vertical normal mode analysis (Kasahara and Puri 1981; Fulton and Schubert 1985) is performed for its determination. The analysis involves two steps. First, a set of vertical normal modes is defined under a given vertical temperature profile. Second, the decomposition is actually applied to the vorticity field with a set of vertical normal modes obtained at the first step.

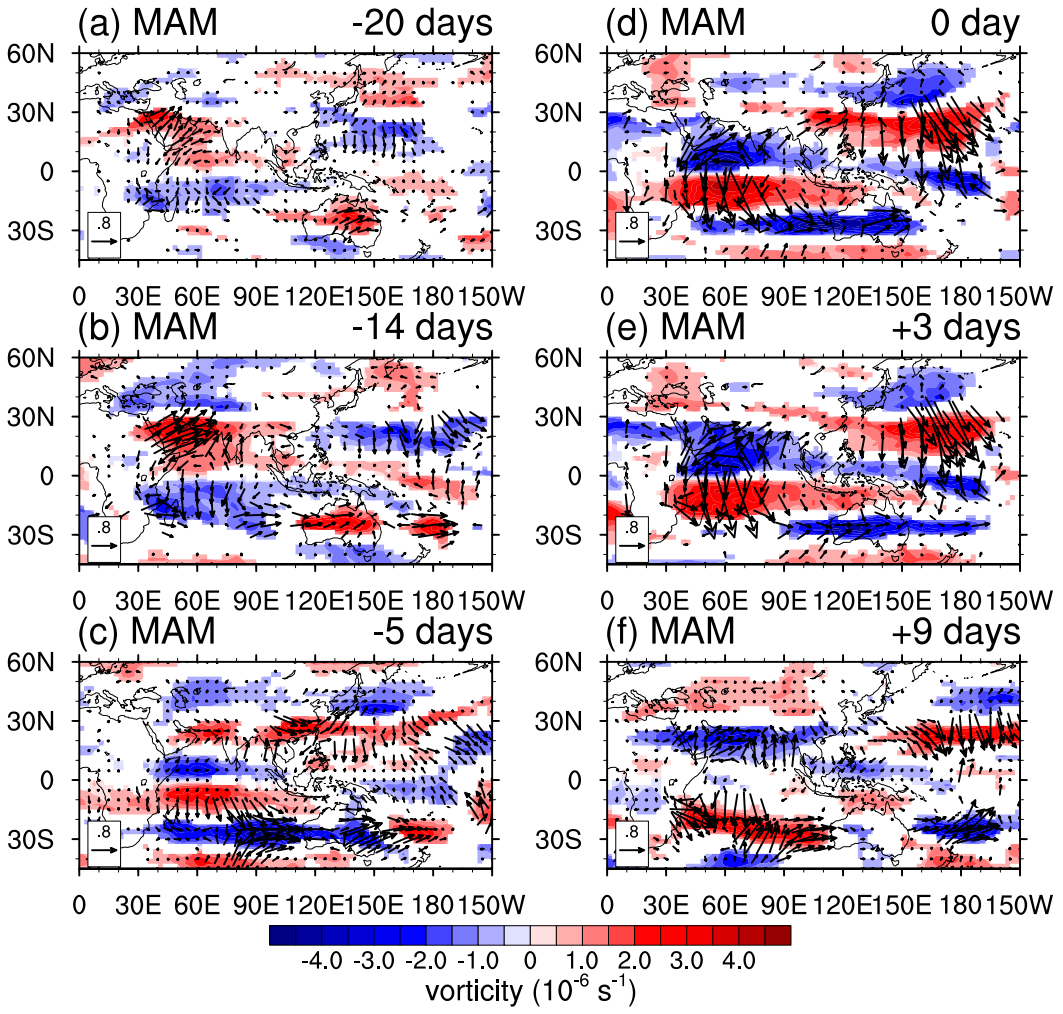

FIG. 14. As in Fig. 12, but for MAM.

A vertical temperature profile required for the first step is defined as an average over the analysis period and over the same domain as for the local analysis in section 3a. This temperature profile is used for evaluating the background static stability as a function of height, a key parameter that is required in solving a differential equation for defining the vertical normal modes. For this purpose, the top of the atmosphere is placed at 0 hPa by setting its temperature value equal to that at 10 hPa. The first step is completed by solving a differential equation that constitutes a Sturm–Liouville problem to obtain the first 40 vertical normal modes (eigenfunctions) and the corresponding equivalent heights as eigenvalues.

The meridionally averaged vorticity in Fig. 17d is then decomposed by these 40 normal modes, and the 40 corresponding expansion coefficients are obtained. The squares of the obtained expansion coefficients are plotted as a function of longitude and equivalent height in Fig. 20: the equivalent barotropic mode with the largest available equivalent height of 10 263.8 m contributes the most to the vertical structure. This result is consistent with a theoretical result by Yano and Tribbia (2017), suggesting a preferred equivalent depth of about 10 km.

4. Discussion and summary

a. General discussion

The 150-hPa vortex-pair structure depicted by the present analysis is fairly comparable to an idealized structure proposed under the modon theory by Yano and Tribbia (2017). Its longitudinal extent is much closer than most of the previous OLR-based analyses to the theoretically expected value of 3000 km. The latitudinal extent confined to 20°S–20°N is also consistent with their theory. This result is contrasted with the composite structure depicted by Hendon and Salby (1994): the vortex scale obtained is much larger (with a longitudinal extent of 70°) due to a heavy spatial filtering applied in

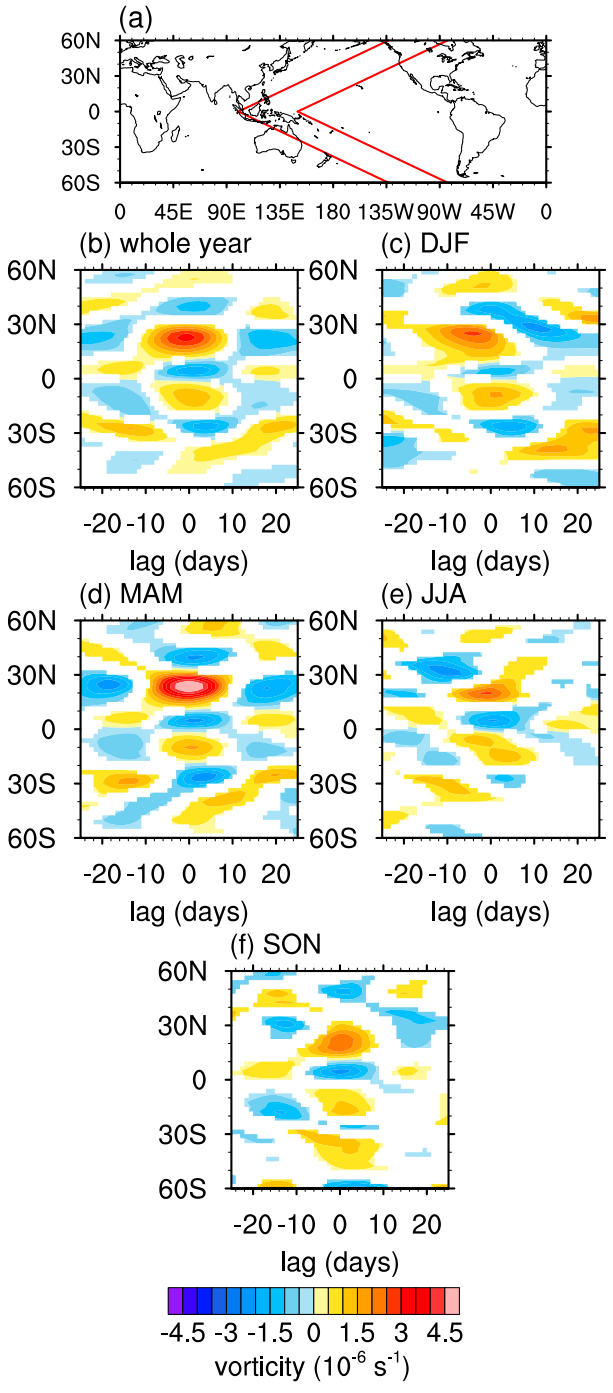

FIG. 15. Slanted time–latitude sections of the lag-regressed vorticity ($\times 10^{-6}\,s^{-1}$) against the third local PC. (a) The longitude range is marked by the red lines. The regression is for (b) the whole year, (c) DJF, (d) MAM, (e) JJA, and (f) SON. Only values above the 99% confidence level are shown.

their analysis. Knutson and Weickmann (1987), Rui and Wang (1990), Kiladis et al. (2005), and Adames and Wallace (2014) have also identified dipolar-vortex structures associated with MJO, however with various

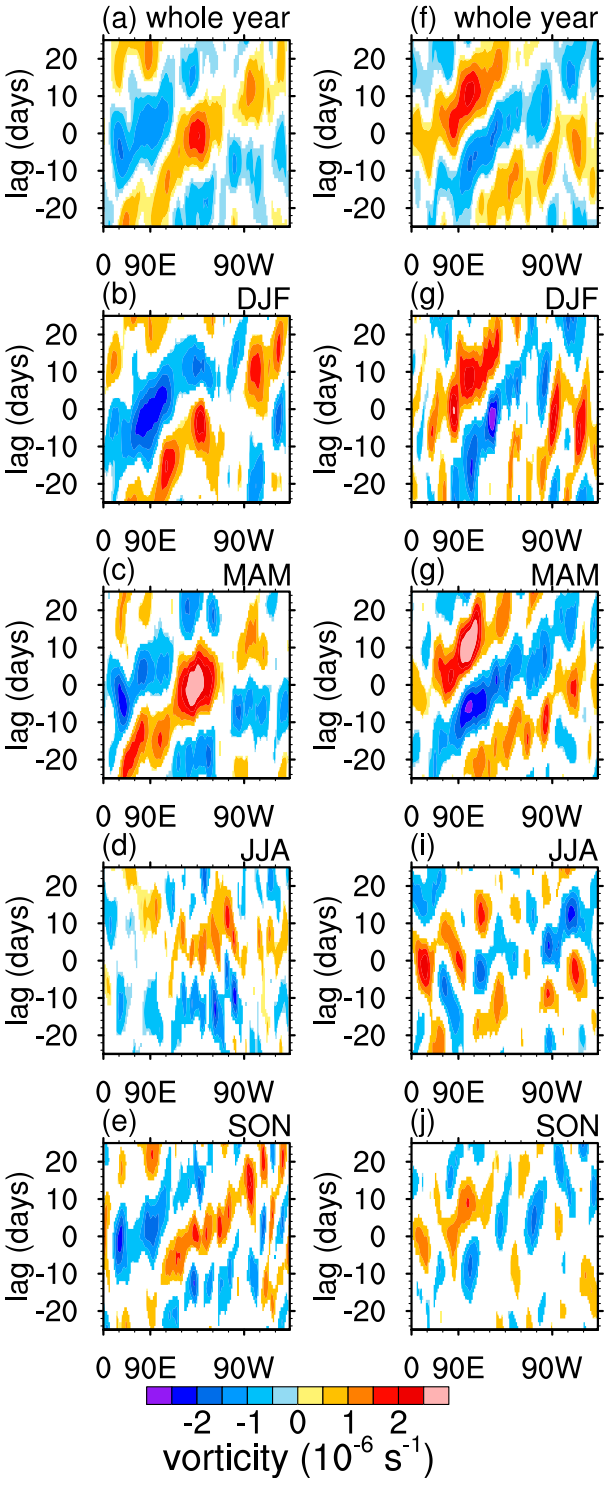

FIG. 16. Time–longitude sections of the lag-regressed vorticity ($\times 10^{-6}\,s^{-1}$) against the third local PC for (a),(f) the whole year, (b),(g) DJF, (c),(g) MAM, (d),(i) JJA, and (e),(j) SON, averaged over (a)–(e) 20°–35°N and (f)–(j) 20°–35°S. Only values above the 99% confidence level are shown.

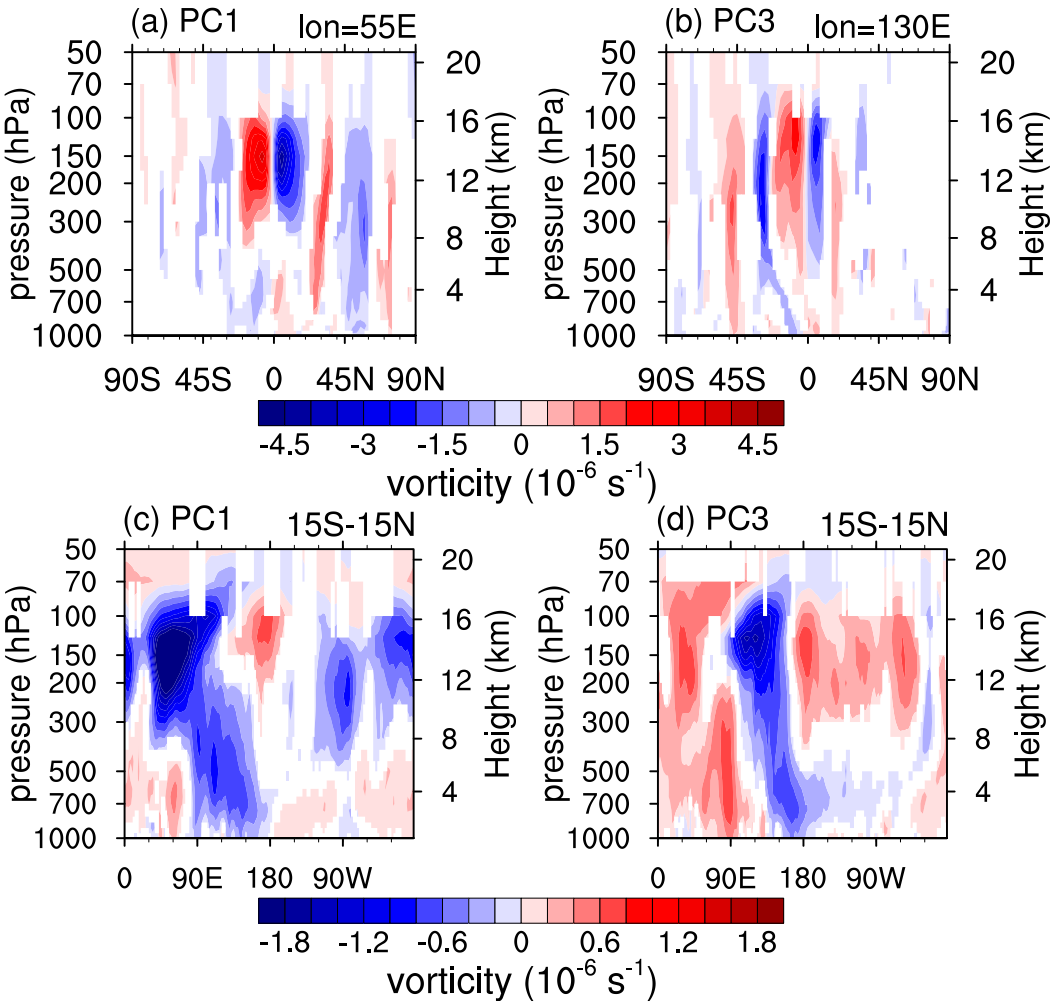

FIG. 17. Height–latitude sections of the simultaneously regressed vorticity ($\times 10^{-6}\,s^{-1}$) against (a) the first local PC at 55°E and (b) the third local PC at 130°E. Height–longitude sections averaged between 15°S and 15°N, with the sign flipped for the Southern Hemisphere, against the (c) first and (d) third local PCs. Only values above the 99% confidence level are shown.

discrepancies with the modon theory. For example, Kiladis et al.'s is too split away from the equator and still too large in horizontal scale in spite of filtering less than Hendon and Salby (1994). The one identified by Adames and Wallace (2014) is slightly smaller in the horizontal scale, but still suffers from the split of the vortex pair away from the equator. These differences in structures are most likely because they use convective activity and related variables as a reference for a composition: the vorticity structure is somehow ''diluted'' as a result.

Interactions of the MJO with the higher-latitude dynamics, as elucidated by the present study, have also been already suggested by various earlier studies. Ray et al. (2009), Zhao et al. (2013), Ray and Li (2013), and Vitart and Jung (2010) suggested an importance of the latitudinal lateral-boundary forcing for simulating the MJO. The present study has more explicitly elucidated the process of Rossby wave trains propagating into the Indian Ocean before an active phase of the MJO by focusing our analysis to the vorticity field at the 150-hPa level.

However, the interactions of the MJO vortex pair with the higher-latitude dynamics turn out to be more complex. It is commonly believed that the convective activity over the tropical western Pacific is a source for the teleconnection pattern stretched from the tropical western Pacific to North America [the so-called Pacific–North American pattern (PNA); cf. Branstator 2014]. It is reasonable to speculate that the MJO is a major such convective source, as suggested by Liebmann and Hartmann (1984), Knutson and Weickmann (1987),

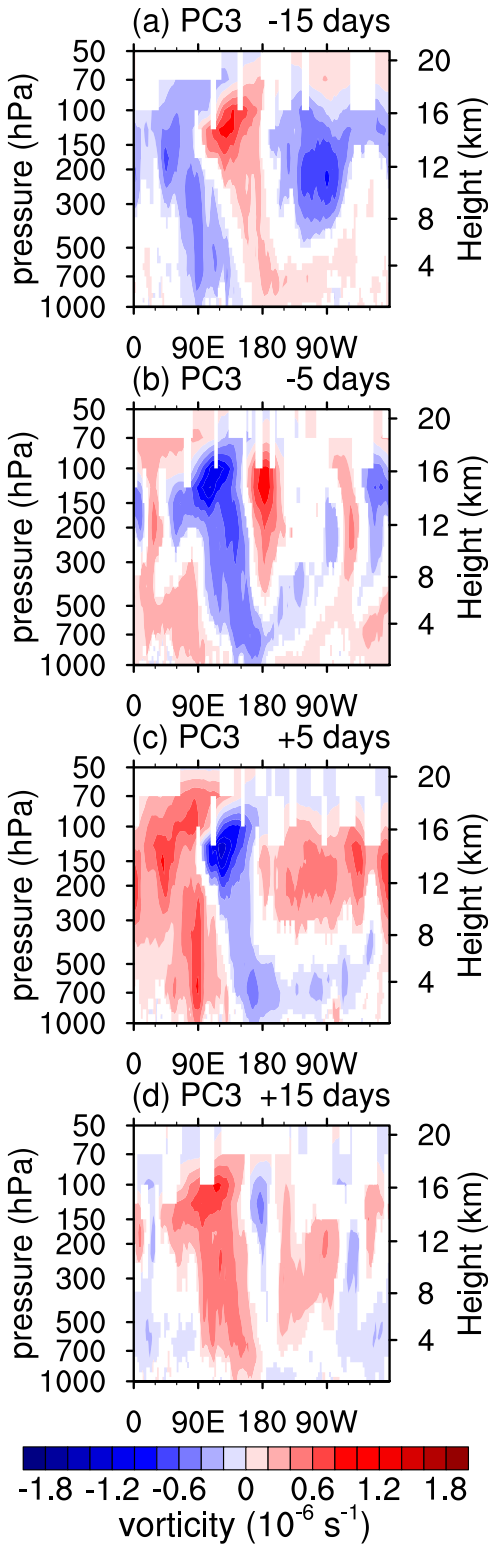

FIG. 18. Height–longitude sections of the regressed vorticity field ($\times 10^{-6}$ s^{-1}), averaged between 15°S and 15°N, with the sign flipped for the Southern Hemisphere, against the third PC for lags (a) −15 to (d) 15 days with a 10-day interval. Only values above the 99% confidence level are shown.

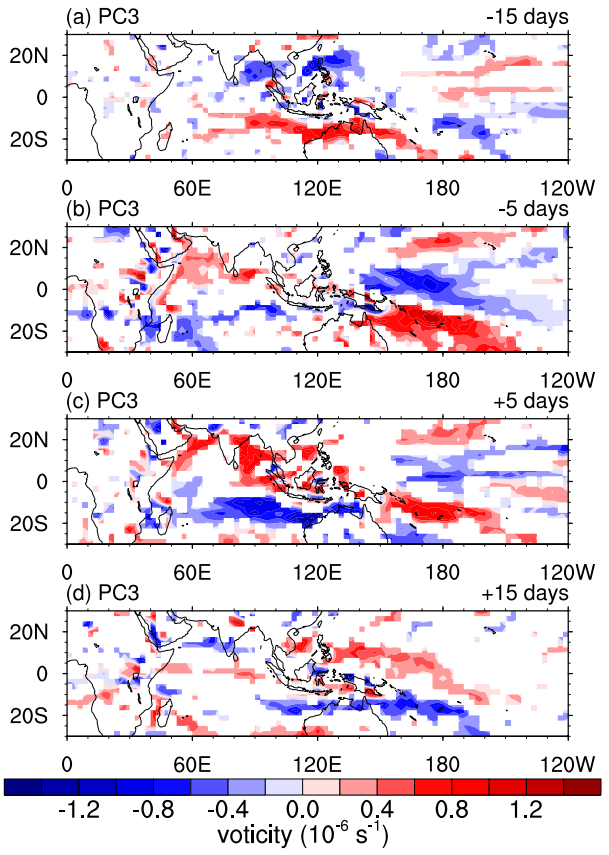

FIG. 19. Regression maps of the vorticity field ($\times 10^{-6}$ s^{-1}) against the third PC at 850 hPa for lags (a) −15 to (d) +15 days with a 10-day interval. Only values above the 99% confidence level are shown.

Matthews et al. (2004), and Kim et al. (2006) from data analysis. The quadrupole vortex structure consisting of the MJO vortex pair over the western Pacific and another vortex pair over the northern Pacific identified as a global MJO mode by our EOF analysis (Fig. 6b) appear to support this view. A similar structure is also identified by Adames and Wallace (2014).

Our time–latitude section analysis (Fig. 15) reveals that these two vortex pairs are spontaneously generated rather than the MJO vortex being preceded by the northern Pacific pair. Our lagged regression analyses (Figs. 12 and 14) suggest that the PNA pattern, or blocking, as represented by the northern Pacific vortex pair, is rather originated from wave activity associated with the MJO over the Indian Ocean. Mori and Watanabe (2008) also suggest the same by tracing Rossby wave trains along PNA backward.

The equivalent barotropic structure of the MJO vortex pair identified by the present study is also a good support of the modon theory based on the equivalent barotropic quasigeostrophic system proposed by

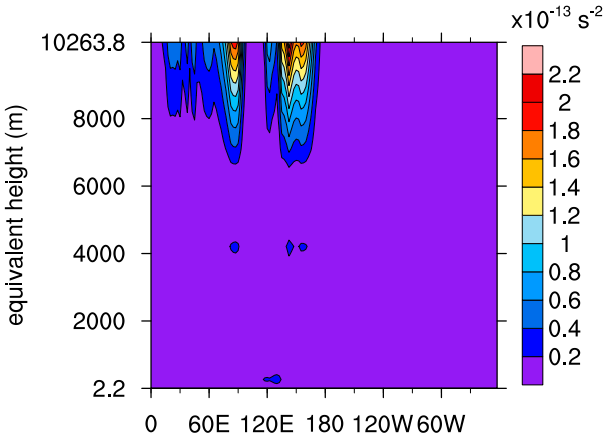

FIG. 20. Expansion coefficients squared ($\times 10^{-13}\,s^{-2}$), obtained by decomposing the vorticity field in Fig. 17d to the first 40 vertical normal modes.

Yano and Tribbia (2017). This finding is also consistent with some previous observational analyses (e.g., Yano et al. 2009; Holloway et al. 2013; Zhang and Ling 2012; Žagar and Franzke 2015). However, unfortunately, this is against a common notion supported by more standard composite analyses, which shows the MJO dominated by the first baroclinic structure (e.g., Hendon and Salby 1994; Kiladis et al. 2005). This contradiction is still left to be resolved by a future study.

b. *Analysis domain*

The present study has focused on the region from the Indian Ocean to the western Pacific, and the process of continuous propagation of the MJO mode crossing the date line eastward has not been considered. Although the original study by Madden and Julian (1972) identified the MJO as a global mode, as the analysis by Milliff and Madden (1996) shows, the continuous mode propagating eastward beyond the date line is clearly identified as a free Kelvin wave. Thus, we better interpret that the main activity of the MJO is confined to the region over the Indian Ocean and the western Pacific. The study has also focused on the intraseasonal scales, and the role of higher-frequency Rossby waves (cf. Matthews and Kiladis 1999), for example, are not considered herein.

c. *The MJO vortex pair as a convectively forced entity?*

The basic premise of the present study is to interpret the MJO vortex pair primarily as a nonlinear free Rossby wave. On the other hand, the observed vortex pair associated with MJO is commonly considered a direct consequence of convection.

The best-known classical approach for describing the response of the large-scale tropical atmosphere to convective heating is to take Gill's (1980) model: it creates a nice dipolar vortex, akin to those identified by EOFs in the present study. However, it is often forgotten that Gill's model is unrealistic, not because of a linear assumption, but crucially, by assuming an unrealistically strong damping rate for both the heat and the momentum equations, as explicitly pointed out in the introduction of Lindzen and Nigam (1987). Once these unrealistically strong dampings are relaxed, the vorticity response is much elongated in longitude, and no longer as compact as observationally identified in the present study.

Monteiro et al. (2014) investigate this issue more carefully: they still take a shallow-water system as the case of Gill (1980), but under a fully nonlinear formulation with a more realistic boundary layer parameterization. Their result is intriguing in the sense that the generated vortex pair is more separated away from the equator compared to the equatorially trapped vortex pair observationally identified. This discrepancy suggests that the vortex pair identified in the present study is likely not properly explained by convective heating centered on the equator. The vortex pair observationally identified by Adames and Wallace (2014) is also split away from the equator, presumably because of the divergent field used for regression. This result is also consistent with the interpretation just stated.

d. *Summary*

Yano and Tribbia (2017) proposed that the strongly nonlinear free-modon solution (Tribbia 1984; Verkley 1984) explains a slow eastward propagation of the MJO. They found that the phase speed of the most stable solution of the Rossby vortex pair is 8–18 $m\,s^{-1}$ with a horizontal scale of 3000 km. However, the identified horizontal scale is rather small compared to previous observational studies by, for example, Hendon and Salby (1994), Kiladis et al. (2005), and Adames and Wallace (2014) taking a convective field or a divergent field as a reference variable for identifying the MJO. In the present study, on the other hand, we have sought to identify the MJO directly in the vorticity field. The 150-hPa pressure level is chosen primarily for the analysis, because such a dipolar-vortex structure is most easily visually identified at this level, as shown in Fig. 1 of Yano and Tribbia (2017). For isolating the MJO signal, the annual cycle and the first three subharmonics are removed, and a 20–200-day bandpass filter is subsequently applied to the vorticity field, by following Matthews (2000). The EOF analysis is then performed on the 150-hPa tropical vorticity field over the Eastern Hemisphere. The two EOF patterns (Figs. 1a,c) are identified as a pair of MJO signals, which constitute an eastward-propagating modon-like vortex pair along the

equator. The vortex pair is well trapped within 20°S and 20°N and has a longitudinal span of about 4500–6000 km, closer than most of the previous studies to the horizontal scale predicted by Yano and Tribbia (2017).

The identified vortex pair is shown to be related to the MJO convective activity by performing a regression analysis against the OLR. The distinguished nature of the vortex pair identified by the present study may be emphasized compared to those found by earlier studies by Hendon and Salby (1994), Rui and Wang (1990), Kiladis et al. (2005), and Adames and Wallace (2014): it is well trapped to the equator and more compact in its longitudinal extent. Its vertical structure is also consistent with the theory that the equivalent height of a dominant mode is about 10 km.

The identified EOF pair is further used for investigating the evolution of the global vorticity field. Some evidence of the interaction of the MJO vortex pair with the subtropical and extratropical Rossby waves are found. The corresponding global EOF patterns with the local EOF pair are identified by searching the best correlations of these two local EOF time series with a whole set of global EOF time series. Identified extratropical structures include a pronounced vortex pair over the North Pacific and a Rossby wave train along a great circle path in the Southern Hemisphere. The evolution of the global vorticity field is further examined by lag regressions. A structure suggesting Rossby wave trains arriving at the Indian Ocean from the Northern Hemisphere to "trigger" the MJO, as suggested by Hsu et al. (1990), Gustafson and Weare (2004), Ray and Zhang (2010), Ray and Li (2013), and Zhao et al. (2013), is identified. The wave activity flux analysis, however, suggests a more complex picture for the whole process. As the vortex pair forms in the Indian Ocean and propagates toward the western Pacific, wave–vortex trains are emitted poleward, which propagate eastward around the zonal circle near 30°N and 30°S in about 50 days (cf. Madden 1978). The seasonal characters of the evolution of the global vorticity field and the eastward propagation of the MJO vortex pair are also investigated, with the weakest signal occurring in summer (JJA).

Many of the features delineated by the present analysis may already be identified by earlier studies to some extent. However, the main innovation of the present study is to show that it is possible to identify an eastward-propagating feature associated with the MJO by taking the vorticity as a reference variable. The analysis is not without further advantages: it has shown the interactions of the MJO vortex pair with higher-latitude vorticity variabilities, through the Rossby wave trains, much more vividly than previous studies. The present study suggests that the MJO is under more active interactions with the higher-latitude Rossby wave dynamics than previously thought. It may even turn out that the MJO may better be understood as a product of interactions with these Rossby waves rather than relatively isolated tropical phenomena. In this respect, the modon theory proposed by Yano and Tribbia (2017) may best be considered a highly idealized picture of a full complexity of the MJO. Such a full picture will emerge only by further investigation. Reznik and Zeitlin (2007, 2009) perform theoretical investigations toward this direction, and we expect more theoretical and observational studies will follow.

Acknowledgments. We particularly thank Grant Brandstettar for suggesting to us the lag-regression analysis. Discussions with George Kiladis, Haiyang Tung, and Nedjeljeka Zagar for various occasions are also acknowledged. The vertical normal mode analysis is built upon a code originally provided by Nedjeljka Zagar. This work was supported by the National Key Research Project of China (Grant 2018YFC1507001).

REFERENCES

Adames, Á. F., and J. M. Wallace, 2014: Three-dimensional structure and evolution of the MJO and its relation to the mean flow. *J. Atmos. Sci.*, **71**, 2007–2026, https://doi.org/10.1175/JAS-D-13-0254.1.

——, J. Patoux, and R. C. Foster, 2014: The contribution of extratropical waves to the MJO wind field. *J. Atmos. Sci.*, **71**, 155–176, https://doi.org/10.1175/JAS-D-13-084.1.

Branstator, G., 2014: Long-lived response of the midlatitude circulations and storm tracks of pulses of tropical heating. *J. Climate*, **27**, 8809–8826, https://doi.org/10.1175/JCLI-D-14-00312.1.

Charney, J. G., 1963: A note on large-scale motions in the tropics. *J. Atmos. Sci.*, **20**, 607–609, https://doi.org/10.1175/1520-0469(1963)020<0607:ANOLSM>2.0.CO;2.

Dee, D. P., and Coauthors, 2011: The ERA-Interim reanalysis: Configuration and performance of the data assimilation system. *Quart. J. Roy. Meteor. Soc.*, **137**, 553–597, https://doi.org/10.1002/qj.828.

Dole, R. M., and N. D. Gordon, 1983: Persistent anomalies of the extratropical Northern Hemisphere wintertime circulation: Geographical distribution and regional persistence characteristics. *Mon. Wea. Rev.*, **111**, 1567–1586, https://doi.org/10.1175/1520-0493(1983)111<1567:PAOTEN>2.0.CO;2.

Emanuel, K. A., 1987: An air–sea interaction model of intraseasonal oscillations in the tropics. *J. Atmos. Sci.*, **44**, 2324–2340, https://doi.org/10.1175/1520-0469(1987)044<2324:AASIMO>2.0.CO;2.

Fuchs, Ž., and D. J. Raymond, 2007: A simple, vertically resolved model of tropical disturbances with a humidity closure. *Tellus*, **59A**, 344–354, https://doi.org/10.1111/j.1600-0870.2007.00230.x.

Fulton, S. R., and W. H. Schubert, 1985: Vertical normal mode transforms: Theory and application. *Mon. Wea. Rev.*, **113**, 647–658, https://doi.org/10.1175/1520-0493(1985)113<0647:VNMTTA>2.0.CO;2.

Gill, A. E., 1980: Some simple solutions for heat-induced tropical circulation. *Quart. J. Roy. Meteor. Soc.*, **106**, 447–462, https://doi.org/10.1002/qj.49710644905.

Gustafson, W. I., Jr., and B. C. Weare, 2004: MM5 modeling of the Madden–Julian oscillation in the Indian and West Pacific Oceans: Model description and control run results. *J. Climate*, **17**, 1320–1337, https://doi.org/10.1175/1520-0442(2004)017<1320:MMOTMO>2.0.CO;2.

Hendon, H. H., and M. L. Salby, 1994: The life cycle of the Madden–Julian oscillation. *J. Atmos. Sci.*, **51**, 2225–2237, https://doi.org/10.1175/1520-0469(1994)051<2225:TLCOTM>2.0.CO;2.

Holloway, C. E., S. J. Woolnough, and G. M. S. Lister, 2013: The effects of explicit versus parameterized convection on the MJO in a large-domain high-resolution tropical case study. Part I: Characterization of large-scale organization and propagation. *J. Atmos. Sci.*, **70**, 1342–1369, https://doi.org/10.1175/JAS-D-12-0227.1.

Hoskins, B. J., and D. J. Karoly, 1981: The steady linear response of a spherical atmosphere to thermal and orographic forcing. *J. Atmos. Sci.*, **38**, 1179–1196, https://doi.org/10.1175/1520-0469(1981)038<1179:TSLROA>2.0.CO;2.

Hsu, H.-H., B. J. Hoskins, and F.-F. Jin, 1990: The 1985/86 intraseasonal oscillation and the role of the extratropics. *J. Atmos. Sci.*, **47**, 823–839, https://doi.org/10.1175/1520-0469(1990)047<0823:TIOATR>2.0.CO;2.

Jiang, X., T. Li, and B. Wang, 2004: Structures and mechanisms of the northward propagating boreal summer intraseasonal oscillation. *J. Climate*, **17**, 1022–1039, https://doi.org/10.1175/1520-0442(2004)017<1022:SAMOTN>2.0.CO;2.

Kasahara, A., and K. Puri, 1981: Spectral representation of three-dimensional global data by expansion in normal mode functions. *Mon. Wea. Rev.*, **109**, 37–51, https://doi.org/10.1175/1520-0493(1981)109<0037:SROTDG>2.0.CO;2.

Kiladis, G. N., and K. M. Weickmann, 1992: Circulations anomalies associated with tropical convection during northern winter. *Mon. Wea. Rev.*, **120**, 1900–1923, https://doi.org/10.1175/1520-0493(1992)120<1900:CAAWTC>2.0.CO;2.

——, K. H. Straub, and P. T. Haertel, 2005: Zonal and vertical structure of the Madden–Julian oscillation. *J. Atmos. Sci.*, **62**, 2790–2809, https://doi.org/10.1175/JAS3520.1.

——, J. Dias, K. H. Straub, M. C. Wheeler, S. N. Tulich, K. Kikuchi, K. M. Weickmann, and M. J. Ventrice, 2014: A comparison of OLR and circulation-based indices for tracking the MJO. *Mon. Wea. Rev.*, **142**, 1697–1715, https://doi.org/10.1175/MWR-D-13-00301.1.

Kim, B. M., G. H. Lim, and K. Y. Kim, 2006: A new look at the midlatitude–MJO teleconnection in the Northern Hemisphere winter. *Quart. J. Roy. Meteor. Soc.*, **132**, 485–503, https://doi.org/10.1256/qj.04.87.

Knutson, T. R., and K. M. Weickmann, 1987: 30–60 day atmospheric oscillations: Composite life cycles of convection and circulation anomalies. *Mon. Wea. Rev.*, **115**, 1407–1436, https://doi.org/10.1175/1520-0493(1987)115<1407:DAOCLC>2.0.CO;2.

Liebmann, B., and D. Hartmann, 1984: An observational study of tropical–midlatitude interaction on intraseasonal time scales during winter. *J. Atmos. Sci.*, **41**, 3333–3350, https://doi.org/10.1175/1520-0469(1984)041<3333:AOSOTI>2.0.CO;2.

——, and C. A. Smith, 1996: Description of a complete (interpolated) outgoing longwave radiation dataset. *Bull. Amer. Meteor. Soc.*, **77**, 1275–1277, https://doi.org/10.1175/1520-0477-77.6.1274.

Lindzen, R. S., and S. Nigam, 1987: On the role of sea surface temperature gradients in forcing low-level winds and convergence in the tropics. *J. Atmos. Sci.*, **44**, 2418–2436, https://doi.org/10.1175/1520-0469(1987)044<2418:OTROSS>2.0.CO;2.

Madden, R. A., 1978: Further evidence of traveling planetary waves. *J. Atmos. Sci.*, **35**, 1605–1618, https://doi.org/10.1175/1520-0469(1978)035<1605:FEOTPW>2.0.CO;2.

——, and P. R. Julian, 1972: Description of global-scale circulation cells in the tropics with a 40–50 day period. *J. Atmos. Sci.*, **29**, 1109–1123, https://doi.org/10.1175/1520-0469(1972)029<1109:DOGSCC>2.0.CO;2.

Majda, A. J., and S. N. Stechmann, 2009: A simple dynamical model with features of convective momentum transport. *J. Atmos. Sci.*, **66**, 373–392, https://doi.org/10.1175/2008JAS2805.1.

Matthews, A. J., 2000: Propagation mechanisms for the Madden-Julian oscillation. *Quart. J. Roy. Meteor. Soc.*, **126**, 2637–2651, https://doi.org/10.1002/qj.49712656902.

——, and G. N. Kiladis, 1999: The tropical–extratropical interaction between high-frequency transients and the Madden–Julian oscillation. *Mon. Wea. Rev.*, **127**, 661–677, https://doi.org/10.1175/1520-0493(1999)127<0661:TTEIBH>2.0.CO;2.

——, B. Hoskins, and M. Masutani, 2004: The global response to tropical heating in the Madden–Julian oscillation during the northern winter. *Quart. J. Roy. Meteor. Soc.*, **130**, 1991–2011, https://doi.org/10.1256/qj.02.123.

Milliff, R. F., and R. A. Madden, 1996: The existence and vertical structure of fast, eastward-moving disturbances in the equatorial troposphere. *J. Atmos. Sci.*, **53**, 586–597, https://doi.org/10.1175/1520-0469(1996)053<0586:TEAVSO>2.0.CO;2.

Monteiro, J. M., Á. F. Adames, J. M. Wallace, and J. S. Sukhatme, 2014: Interpreting the upper-level structure of the Madden–Julian oscillation. *Geophys. Res. Lett.*, **41**, 9158–9165, https://doi.org/10.1002/2014GL062518.

Mori, M., and M. Watanabe, 2008: The growth and triggering mechanisms of the PNA: A MJO-PNA coherence. *J. Meteor. Soc. Japan*, **86**, 213–236, https://doi.org/10.2151/jmsj.86.213.

Murakami, T., 1987: Intraseasonal atmospheric teleconnection patterns during the Northern Hemisphere summer. *Mon. Wea. Rev.*, **115**, 2133–2154, https://doi.org/10.1175/1520-0493(1987)115<2133:IATPDT>2.0.CO;2.

——, 1988: Intraseasonal atmospheric teleconnection patterns during the Northern Hemisphere winter. *J. Climate*, **1**, 117–131, https://doi.org/10.1175/1520-0442(1988)001<0117:IATPDT>2.0.CO;2.

Nishi, N., 1989: Observational study on the 30–60 day variations in the geopotential and temperature fields in the equatorial region. *J. Meteor. Soc. Japan*, **67**, 187–203, https://doi.org/10.2151/jmsj1965.67.2_187.

Ray, P., and C. Zhang, 2010: A case study of the mechanics of extratropical influence on the initiation of the Madden–Julian oscillation. *J. Atmos. Sci.*, **67**, 515–528, https://doi.org/10.1175/2009JAS3059.1.

——, and T. Li, 2013: Relative roles of circumnavigating waves and extratropics on the MJO and its relationship with the mean state. *J. Atmos. Sci.*, **70**, 876–893, https://doi.org/10.1175/JAS-D-12-0153.1.

——, C. Zhang, J. Dudhia, and S. S. Chen, 2009: A numerical case study on the initiation of the Madden–Julian oscillation. *J. Atmos. Sci.*, **66**, 310–331, https://doi.org/10.1175/2008JAS2701.1.

Raymond, D. J., and Ž. Fuchs, 2007: Convectively coupled gravity and moisture modes in a simple atmospheric model. *Tellus*, **59A**, 627–640, https://doi.org/10.1111/j.1600-0870.2007.00268.x.

——, and ——, 2009: Moisture modes and the Madden–Julian oscillation. *J. Climate*, **22**, 3031–3046, https://doi.org/10.1175/2008JCLI2739.1.

Reznik, G. M., and V. Zeitlin, 2007: Interaction of free Rossby waves with semi-transparent equatorial waveguides. Part 1.

Wave triads. *Physica D*, **226**, 55–79, https://doi.org/10.1016/j.physd.2006.11.003.

——, and ——, 2009: Interaction of free Rossby waves with semi-transparent equatorial waveguides—Wave–mean flow interaction. *Nonlinear Processes Geophys.*, **16**, 381–392, https://doi.org/10.5194/npg-16-381-2009.

Rostami, M., and V. Zeitlin, 2019: Eastward-moving convection-enhanced modons in shallow water in the equatorial tangent plane featured. *Phys. Fluids*, **31**, 021701, https://doi.org/10.1063/1.5080415.

Rui, H., and B. Wang, 1990: Development characteristics and dynamic structure of tropical intraseasonal convection anomalies. *J. Atmos. Sci.*, **47**, 357–379, https://doi.org/10.1175/1520-0469(1990)047<0357:DCADSO>2.0.CO;2.

Salby, M. L., and H. H. Hendon, 1994: Intraseasonal behavior of clouds, temperature, and motion in the tropics. *J. Atmos. Sci.*, **51**, 2207–2224, https://doi.org/10.1175/1520-0469(1994)051<2207:IBOCTA>2.0.CO;2.

Small, D., E. Atallah, and J. R. Gyakum, 2014: An objectively determined blocking index and its Northern Hemisphere climatology. *J. Climate*, **27**, 2948–2970, https://doi.org/10.1175/JCLI-D-13-00374.1.

Takaya, K., and H. Nakamura, 2001: A formulation of a phase-independent wave-activity flux for stationary and migratory quasigeostrophic eddies on a zonally varying basic flow. *J. Atmos. Sci.*, **58**, 608–627, https://doi.org/10.1175/1520-0469(2001)058<0608:AFOAPI>2.0.CO;2.

Tribbia, J. J., 1984: Modons in spherical geometry. *Geophys. Astrophys. Fluid Dyn.*, **30**, 131–168, https://doi.org/10.1080/03091928408210080.

Ventrice, M. J., M. C. Wheeler, H. H. Hendon, I. Schreck, J. Carl, C. D. Thorncroft, and G. N. Kiladis, 2013: A modified multivariate Madden–Julian oscillation index using velocity potential. *Mon. Wea. Rev.*, **141**, 4197–4210, https://doi.org/10.1175/MWR-D-12-00327.1.

Verkley, W. T. M., 1984: The construction of barotropic modons on a sphere. *J. Atmos. Sci.*, **41**, 2492–2504, https://doi.org/10.1175/1520-0469(1984)041<2492:TCOBMO>2.0.CO;2.

Vitart, F., and T. Jung, 2010: Impact of the Northern Hemisphere extratropics on the skill in predicting the Madden Julian oscillation. *Geophys. Res. Lett.*, **37**, L23805, https://doi.org/10.1029/2010GL045465.

Weickmann, K. M., G. R. Lussky, and J. E. Kutzbach, 1985: Intraseasonal (30–60 day) fluctuations of outgoing longwave radiation and 250 mb streamfunction during northern winter. *Mon. Wea. Rev.*, **113**, 941–961, https://doi.org/10.1175/1520-0493(1985)113<0941:IDFOOL>2.0.CO;2.

Wheeler, M. C., and H. H. Hendon, 2004: An all-season real-time multivariate MJO index: Development of an index for monitoring and prediction. *Mon. Wea. Rev.*, **132**, 1917–1932, https://doi.org/10.1175/1520-0493(2004)132<1917:AARMMI>2.0.CO;2.

Yanai, M., B. Chen, and W.-W. Tung, 2000: The Madden–Julian oscillation observed during the TOGA COARE IOP: Global view. *J. Atmos. Sci.*, **57**, 2374–2396, https://doi.org/10.1175/1520-0469(2000)057<2374:TMJOOD>2.0.CO;2.

Yano, J.-I., and K. A. Emanuel, 1991: An improved model of the equatorial troposphere and its coupling with the stratosphere. *J. Atmos. Sci.*, **48**, 377–389, https://doi.org/10.1175/1520-0469(1991)048<0377:AIMOTE>2.0.CO;2.

——, and M. Bonazzola, 2009: Scale analysis for large-scale tropical atmospheric dynamics. *J. Atmos. Sci.*, **66**, 159–172, https://doi.org/10.1175/2008JAS2687.1.

——, and J. J. Tribbia, 2017: Tropical atmospheric Madden–Julian oscillation: Strongly nonlinear free solitary Rossby wave? *J. Atmos. Sci.*, **74**, 3473–3489, https://doi.org/10.1175/JAS-D-16-0319.1.

——, S. Mulet, and M. Bonazzola, 2009: Tropical large-scale circulations: Asymptotically non-divergent? *Tellus*, **61A**, 417–427, https://doi.org/10.1111/j.1600-0870.2009.00397.x.

Yasunari, T., 1979: Cloudiness fluctuations associated with the Northern Hemisphere summer monsoon. *J. Meteor. Soc. Japan*, **57**, 227–229, https://doi.org/10.2151/jmsj1965.57.3_227.

——, 1980: A quasi-stationary appearance of 30 to 40 day period in the cloudiness fluctuations during the summer monsoon over India. *J. Meteor. Soc. Japan*, **58**, 225–229, https://doi.org/10.2151/jmsj1965.58.3_225.

——, 1981: Structure of an Indian summer monsoon system with around 40-day period. *J. Meteor. Soc. Japan*, **59**, 336–354, https://doi.org/10.2151/jmsj1965.59.3_336.

Žagar, N., and C. L. E. Franzke, 2015: Systematic decomposition of the Madden–Julian oscillation into balanced and inertia-gravity components. *Geophys. Res. Lett.*, **42**, 6829–6835, https://doi.org/10.1002/2015GL065130.

Zhang, C., 2005: Madden–Julian oscillation. *Rev. Geophys.*, **43**, RG2003, https://doi.org/10.1029/2004RG000158.

——, and M. Dong, 2004: Seasonality in the Madden–Julian oscillation. *J. Climate*, **17**, 3169–3180, https://doi.org/10.1175/1520-0442(2004)017<3169:SITMO>2.0.CO;2.

——, and J. Ling, 2012: Potential vorticity of the Madden–Julian oscillation. *J. Atmos. Sci.*, **69**, 65–78, https://doi.org/10.1175/JAS-D-11-081.1.

Zhao, C., T. Li, and T. Zhou, 2013: Precursor signals and processes associated with MJO initiation over the tropical Indian Ocean. *J. Climate*, **26**, 291–307, https://doi.org/10.1175/JCLI-D-12-00113.1.